Lattice Boltzmann k-ω SST based hybrid RANS/LES simulations of turbulent flows

Sajad Mozaffari, Shang-Gui Cai, Jérôme Jacob, Pierre Sagaut

Lattice Boltzmann k-ω SST based hybrid RANS/LES simulations of turbulent flows

Sajad Mozaffari[a], Shang-Gui Cai[b,c,a,*], Jérôme Jacob[a] and Pierre Sagaut[a]

[a]Aix Marseille Univ, CNRS, Centrale Marseille, M2P2 UMR 7340, 38 rue Joliot-Curie, 13451, Marseille, France
[b]Key Laboratory for Mechanics in Fluid Solid Coupling Systems, Institute of Mechanics, Chinese Academy of Sciences, Beijing 100190, China
[c]School of Engineering Science, University of Chinese Academy of Sciences, Beijing 100049, China

ARTICLE INFO

Keywords:
Hybrid RANS/LES
Lattice Boltzmann Method (LBM)
Turbulence modeling
High Reynolds numbers

ABSTRACT

High Reynolds number simulations with lattice Boltzmann method (LBM) have been computationally feasible by means of turbulence models for under-resolved physical scales. Hybrid RANS/LES models are efficient alternatives to accurate but computationally expensive LES techniques. This study investigates extensively the hybrid RANS/LES models in the LBM framework for complex wall-bounded turbulent flow simulations on non-body fitting Cartesian grids. The hybridization processes for these models are applied to a widely used two-equation RANS base model, specifically the k-ω SST turbulence model. The functionality of these hybrid models is validated through the simulation of a three-dimensional fully turbulent flow over an airfoil. In addition, they are assessed by performing LBM simulations of flows surrounding a generic vehicle geometry, the Ahmed body, in order to reproduce the solution of a similar simulation by conventional CFD methods and to compare with wind tunnel experimental data. It is found that the near-wall treatments have significant impacts on the local boundary flow structures and possible remedies are also discussed.

1. Introduction

The lattice Boltzmann method (LBM), as a mesoscopic computational approach, has received considerable attention in recent years for high Reynolds number, moderate Mach number aerodynamic simulations. The challenges in the conventional Navier-Stokes solver lie in the discretization of the nonlinear convective term $(u \cdot \nabla u)$ in the momentum equation and the time-consuming process of solving the Poisson pressure equation. The linearity of system equations in LBM makes it an attractive and efficient method for performing wall-bounded large eddy simulations (LES). The advantages of using LBM rather than Navier-Stokes solvers is highlighted by Marié et al. [38] for aeroacoustic simulation on academcic configuration. Boivin et al. [3] demonstrated higher efficiency of LBM compared to low Mach Navier-Stokes codes in the framework of combustion. Suss et al. [52] analyzed the properties of these two methods in terms of accuracy and computational cost, showing that LBM is more efficient when dealing with simulations of shear driven flows. The turbulence simulation capability of LBM can be expanded by incorporating turbulence models. Various turbulence models have been used alongside this method so far in different applications. The Smagorinsky model was first proposed as an LES model based on the LBM [25], which later has been extended to more realistic flows [13, 14, 37, 65, 66]. Other LES models including the wall-adapting local eddy-viscosity (WALE) [17] and the Vreman [56] sub-grid scale models were also considered in a generalized LBM-LES framework [5, 36, 59].

Low grid resolution requirement and less computational cost of the Reynolds-Averaged Navier–Stokes (RANS) equations, make them a good option to be performed in steady conditions and/or in two-dimensional domains. The one-equation Spalart-Allmaras (SA) model [48] and the two-equation k-ϵ model have been introduced into the standard LBM framework to simulate relatively high Reynolds number flows [19, 33, 43]. Recently, Wang et al. [58] implemented the k-ω SST turbulence model in non-standard LBM finite volume framework [57] on an unstructured grid. They demonstrated the applicability of the SST model in accurately predicting the incompressible turbulent flows including flow over a backward-facing step and flow around a NACA-0012 airfoil.

For classic RANS computations, simulating unsteady complex flows at high Reynolds numbers is challenging. Local flow separations and the need for an accurate resolution of the unsteady features, make LES computations a

*Corresponding author
sajad.mozaffari@univ-amu.fr (S. Mozaffari); shanggui.cai@imech.ac.cn (S. Cai); jerome.jacob@univ-amu.fr (J. Jacob)
ORCID(s): 0000-0001-6061-4010 (S. Mozaffari); 0000-0002-7406-562X (S. Cai); 0000-0001-9287-4167 (J. Jacob); 0000-0002-3785-120X (P. Sagaut)

better choice for these flows. However, performing LES to resolve near-wall turbulence is still out of reach for currently available computing power. This is due to the need of locally fine grids in the vicinity of the walls to capture small flow features inside boundary layers. Contrarily, resolving these local flow features (e.g. attached boundary layers) is not necessarily useful, since they can be modeled to a satisfactory accuracy at a lower cost using a RANS model. The hybrid RANS/LES concept was introduced by Spalart [47] with the idea of applying LES in the separated flow region to capture the three-dimensional time-dependent flow feature and a RANS model in the attached boundary layers near the wall to avoid excessively fine grids for capturing small-scale flow structures. In recent studies, benefiting from the capabilities of the hybrid RANS/LES turbulence models in the LBM framework has been considered. As the first attempt, hybrid RANS/LES in conjunction with the LBM was investigated for indoor airflow simulations [44]. The hybrid model was based on the two-equation k-ϵ turbulence model by two additional transport equations for the probability distribution function of populations of k and ϵ into the LBM formulation. In another study, Degrigny et al. [12] performed hybrid RANS/LES simulations based on the SA turbulence model in standard LBM computations on an airfoil profile. Nevertheless, as opposed to traditional hybrid RANS-LES on body-fitting grids, using Cartesian grid based LBM for complex turbulent flow simulations remains highly unexplored.

In this study, the performance and the reliability of two k-ω SST based hybrid RANS/LES models in combination with LBM are investigated by the simulation of aerodynamic external flows at high Reynolds number over complex geometries on Cartesian grids. This work uses the LBM solver ProLB, which is introduced in Section 2 along with a brief description of the lattice Boltzmann method and the near-wall treatment. In the following, the formulation and implementation of turbulence models including the k-ω SST RANS model, the improved delayed detached eddy simulation (IDDES), and the continuous eddy simulation (CES) are described as well. In Section 3.1, since the k-ω SST turbulence model has never been used in the standard LBM framework, the performance of the k-ω SST model is first compared to the SA model which has been used reliably with LBM in ProLB for a 2D airfoil [6, 62]. Afterward, in Section 3.2, the hybrid models are tested by simulating turbulent flow over a 3D airfoil, taking into account the three-dimensional effects of turbulence. The effectiveness of the hybrid RANS/LES methods is then evaluated for the simulation of a complex, realistic test case of an Ahmed body in Section 3.3. For all the tests, comparisons with reference simulations and experimental data are conducted to determine whether the turbulence models can reliably simulate such flow cases on non-body fitting Cartesian grids and discussions are finally offered in Section 4.

2. ProLB solver

This study is based on a research version of the commercial LBM solver ProLB [10], developed within a scientific collaboration including CSSI, Renault, Airbus, École Centrale de Lyon, CNRS, and Aix-Marseille University. In this section, a brief description of the lattice Boltzmann method, which is used in this work for the hybrid RANS/LES simulation of unsteady turbulent flows, is given. For a detailed introduction to the fundamental theory of the LBM and its application it is referred to the book by Krüger et al. [29]. In addition, a near-wall treatment is implemented in ProLB solver in order to avoid excessively refined Cartesian grids near a solid boundary in high Reynolds number flows. Several hybrid RANS/LES turbulence models along with their baseline framework, the two-equation k-ω SST RANS model, are also discussed in this section. These turbulence models have been implemented in the ProLB solver and will be validated by simulating highly unsteady flows including separation.

2.1. Lattice Boltzmann method

The LBM is based on the statistical mechanics of particles at a mesoscopic scale. This approach describes the dynamics of a group of particles that collide and propagate over a discrete lattice based on the discrete velocity Boltzmann equation. The physical unknowns of the method are the probability distribution functions $f_i(t, \mathbf{x}, \mathbf{c}_i)$, which describe the probability of encountering a particle with discrete velocities $\mathbf{c}_i$ at location $\mathbf{x}$ and time t. In the ProLB solver, the Boltzmann equation is discretized in a 3D lattice with 19 discrete velocities (D3Q19). Applying the trapezoidal rule to integrate the discrete velocity Boltzmann equation in time, after a change of variable $\bar{f}_i = f_i - \Delta t \Omega_i/2$, gives to an explicit scheme as [15]:

$$\bar{f}_i(t + \Delta t, \mathbf{x} + \mathbf{c}_i \Delta t) - \bar{f}_i(t, \mathbf{x}) = \Delta t \cdot \bar{\Omega}_i(t, \mathbf{x}), \tag{1}$$

where the collision operator $\bar{\Omega}_i(t,\mathbf{x})$, models the interactions of particles as a relaxation towards an equilibrium state f_i^{eq} :

$$\bar{\Omega}_i(t,\mathbf{x}) = -\frac{1}{\bar{\tau}}(\bar{f}_i - f_i^{eq}), \tag{2}$$

where the relaxation time $\bar{\tau} = \tau + 0.5$ is related to the fluid kinematic viscosity ($\tau = \nu/c_s^2$). The Maxwell–Boltzmann equilibrium expanded in Hermite polynomials is given by

$$f_i^{eq} = w_i\rho\left(1 + \frac{\mathbf{u}\cdot\mathbf{c}_i}{c_s^2} + \frac{1}{2c_s^4}\mathbf{H}_i^{(2)} : \mathbf{uu}\right). \tag{3}$$

In Eq. 3, ρ and $\mathbf{u}$ are the density and the velocity of the fluid which are reconstructed using the probability distribution functions. Moreover, w_i is the weighting factor depending on the discrete velocity direction, and the second order Hermite polynomial ($\mathbf{H}_i^{(2)}$), with the identity matrix $\mathbf{I}$, is

$$\mathbf{H}_i^{(2)} = \mathbf{c}_i\mathbf{c}_i - c_s^2\mathbf{I}. \tag{4}$$

Due to the instability of the original collision operator for most practical applications at high Reynolds number flows, by decomposing the distribution function into an equilibrium and a non-equilibrium part ($\bar{f}_i = f_i^{eq} + f_i^{neq}$), a hybrid recursive regularized (HRR) collision operator [26] is developed, which expands the non-equilibrium part of the particle distribution function (f_i^{neq}) into Hermite series and introduces a hyper viscosity, as follow:

$$\bar{\Omega}_i^{HRR}(t,\mathbf{x}) = -\frac{1}{\bar{\tau}}\left(f_i^{neq}\sigma - (1-\sigma)\frac{\rho\tau}{c_s^2}\mathbf{H}_i^{(2)} : \mathbf{S}^{\mathrm{FD}}\right), \tag{5}$$

where $\mathbf{S}^{\mathrm{FD}}$ represents the strain rate tensor that is evaluated using finite difference. As described in Jacob et al. [26], the σ parameter of the HRR model introduces a bi Laplacian based hyper viscosity in the LBM scheme due to the use of a second order centered finite differences scheme for the estimation of the strain rate tensor $\mathbf{S}^{\mathrm{FD}}$. This hyper viscosity improves the stability of the method by increasing the dissipation of non physical modes in the LBM scheme while limiting the dissipation of physical modes allowing for a good accuracy of the model as shown in Astoul et al.[2]. In the present work, $\sigma = 0.98$ is used for the HRR model. It is noteworthy that exploring the impact of different parameters or even collision operators could be a valuable direction for future research to enhance simulation accuracy and stability for turbulent flows, however, it is important to clarify that these aspects are not within the scope of the current study.

Turbulence effects are taken into account in the collision operator through the relaxation time $\bar{\tau}$ towards the equilibrium. The eddy viscosity ν_t, calculated by turbulence models, is introduced in the relaxation time of the regularized collision model as

$$\bar{\tau} = \frac{\Delta t}{2} + \frac{\nu + \nu_t}{c_s^2}, \tag{6}$$

where c_s is the lattice speed of sound.

In LBM, the macroscopic properties of the fluid can be reconstructed from the statistical moments of the particle distributions:

$$\rho(t,\mathbf{x}) = \sum_i \bar{f}_i(t,\mathbf{x}), \tag{7}$$

$$\rho\mathbf{u}(t,\mathbf{x}) = \sum_i \mathbf{c}_i\bar{f}_i(t,\mathbf{x}). \tag{8}$$

.

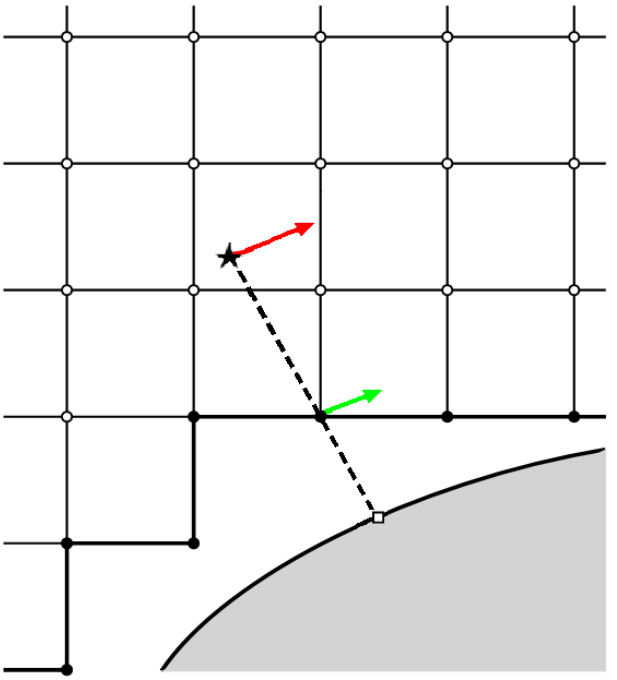

Figure 1: Cartesian grid in LBM and wall treatment strategy to apply the tangential velocity boundary condition; •: boundary node, ○: fluid node, ★: reference point, and □: projected surface points.

2.2. Near-wall treatment

In ProLB, the LBM is implemented on a Cartesian grid which is not body-fitted, as illustrated in Fig. 1. The *boundary nodes* do not necessarily lie on the solid boundary and the LBM scheme is not completed at these off-surface nodes (boundary nodes). Therefore, a reconstruction method should be used to estimate the velocity at the boundary nodes from the velocity predicted at neighboring fluid nodes.

In ProLB, based on the immersed boundary (IBM) approach, several fictitious reference points are established along the wall-normal direction passing the boundary points at a distance of the local grid size successively, which their values are interpolated from the neighbor points [6]. Then, the flow quantities (e.g. velocity or density) at boundary nodes are constructed, linearly or quadratically, based on the boundary type, Dirichlet boundary condition (e.g. inflow velocity, or no-slip velocity), or Neumann boundary condition (e.g. outflow velocity). Thanks to the regularized approach, the macroscopic boundary conditions can be easily transformed into the particle distribution functions for LBM. The equilibrium part is reconstructed from the flow velocity and density, while the non-equilibrium part can be computed from the symmetric part of the velocity gradient tensor. In order to obtain accurate results, advanced gradient schemes have been used on the boundary nodes, cf. [6, 11, 7].

Additionally, for high Reynolds number flows, due to the mesh isotropy in ProLB, it is too expensive to sufficiently refine the grids in the wall-normal direction near a solid boundary in order to explicitly resolve the boundary layer. Therefore, a wall model, based on the tangential velocity at these reference points, can determine the tangential velocity and the quantities related to the turbulence model of the first off-wall node. According to this, the velocity direction matches the tangential velocity at the reference point (Fig. 1, see [62]).

Several wall models are available in ProLB to describe the velocity profile in the turbulent boundary layer by a relation between the tangential velocity, the distance to the wall, and the friction velocity. An algebraic wall model based on a power-law velocity profile was proposed by Wilhelm et al. [62] in which the requirement of an iterative procedure, like in conventional methods, for the determination of the wall shear stress was eliminated. In another attempt, Cai et al. [8] defined an algebraic fully explicit wall model which covers the entire inner region of the turbulent boundary layer to reduce the computational effort for wall-bounded turbulent flows. In both wall models, the boundary layer is assumed to be at equilibrium, and no provision was added for taking into account the effects of adverse pressure gradients. This can impose non-physical perturbations in the case of a boundary layer under an adverse pressure

gradient and in particular for separated boundary layers. Recently, Wilhelm et al. [63] extended their equilibrium power-law wall model for boundary layers under an adverse pressure gradient.

It has been shown by Cai et al. [7] that for fully separated flows, the equilibrium wall model would operate at low y^+ regions that are comparable to linear reconstruction. Therefore, in this work, the fully explicit equilibrium wall model proposed by Cai et al. [8] is considered, and the probable effects of not considering the adverse pressure gradient have been ignored.

The key idea for developing explicit wall models is to express the non-dimensional quantities u^+ or y^+ as a function of the local Reynolds number [8]

$$Re_y = \frac{uy}{\nu} = u^+ y^+, \tag{9}$$

where $u^+ = \frac{u}{u_\tau}$ and $y^+ = \frac{y u_\tau}{\nu}$, with u_τ being the friction velocity, y the distance to the wall, and ν the molecular kinematic viscosity. Therefore, the friction velocity, u_τ, can be evaluated through

$$u_\tau = \frac{u}{u^+\left(Re_y\right)} \quad \text{or} \quad u_\tau = \frac{y^+\left(Re_y\right)\nu}{y}. \tag{10}$$

Dividing the turbulent boundary layer into three parts: the viscous sublayer, the buffer layer, and the inertial layer. For the viscous sublayer,

$$u^+ = y^+ = \sqrt{Re_y}. \tag{11}$$

In the inertial layer, the velocity follows a logarithmic law,

$$u^+ = \frac{1}{\kappa}\log\left(Ey^+\right) \quad \text{or} \quad y^+ = \frac{1}{E}e^{\kappa u^+}, \tag{12}$$

where $\kappa \approx 0.41$ and $E \approx 7.9$. The explicit version of the logarithmic profile in the inertial layer can be built as

$$y^+\left(Re_y\right) = \frac{1}{E}e^{W\left(\kappa E Re_y\right)}, \tag{13}$$

where the Lambert function W is implicitly defined as

$$W\left(\kappa E Re_y\right) = \log\left(\frac{\kappa E Re_y}{W\left(\kappa E Re_y\right)}\right), \tag{14}$$

that can be represented by finite series [8].

Finally, a unified expression for the entire layer can be given in the form [8]

$$\begin{aligned} y^+\left(Re_y\right) &= \left(1-\tanh\frac{Re_y}{s}\right)^p \left(Re_y\right)^{1/2} + \left(\tanh\frac{Re_y}{s}\right)^p \frac{1}{E}e^{W\left(\kappa E Re_y\right)}, \\ u^+\left(Re_y\right) &= \frac{Re_y}{y^+\left(Re_y\right)}, \end{aligned} \tag{15}$$

with $p = 0.7894$ and $s = 86.58$.

2.3. Turbulence models

The ProLB solver was initially developed for performing wall-modeled LES (WMLES) simulations. With the use of a wall model, an LES simulation was feasible for high Reynolds numbers in a computational domain with a non-body-fitted mesh. For the external aerodynamics applications, a Spallart-Almaras RANS turbulence model was also validated for this solver [6, 11, 62], and has been widely used. The robustness of the two-equation RANS model, especially k-ω SST, and its wide range of applications for the attached flows, attract attention to the hybrid RANS/LES turbulence model. Therefore, in this study, the hybridization methods discussed below are applied to the base model of k-ω SST.

k-ω Shear-Stress Transport (SST).

The k-ω turbulence model is one of the most commonly used models to capture more precisely the effect of turbulent flow conditions. It belongs to the Reynolds-averaged Navier-Stokes (RANS) family of turbulence models where all the effects of turbulence are modeled. There exist different variations of the k-ω model such as the standard k-ω [60], the baseline k-ω [61], the SST k-ω [40], etc., each with some modifications to perform better under certain conditions of the fluid flow. However, all these models have similar forms, with transport equations for the turbulence kinetic energy, k, and the specific dissipation rate, ω.

One of the weak points of the earlier k-ω turbulence model is the sensitivity of the solutions to values of k and ω outside the shear layer (freestream sensitivity), especially for free shear flows [41]. To solve this issue, in the SST k-ω model [40], the robust and accurate formulation of the k-ω model in the near-wall region is effectively blended with the freestream independence formulation of the k-ϵ model in the far field. In addition, the definition of turbulent viscosity was modified to account for the transport effects of the principal turbulent shear stress. These features make the SST k-ω model more accurate and reliable for a wider class of flows (for example, adverse pressure gradient flows, airfoils, transonic shock waves) than the earlier versions of k-ω.

The equations for the turbulence kinetic energy k $[m^2/s^2]$ and the specific turbulent dissipation ω $[1/s]$ are the following:

$$\frac{\partial k}{\partial t} + \frac{\partial (u_j k)}{\partial x_j} = \tau_{ij}\frac{\partial u_j}{\partial x_j} - \beta^* \omega k + \frac{\partial}{\partial x_j}\left[\left(\nu + \sigma_k \nu_t\right)\frac{\partial k}{\partial x_j}\right], \tag{16}$$

$$\frac{\partial \omega}{\partial t} + \frac{\partial (u_j \omega)}{\partial x_j} = \frac{\gamma}{\nu_t}\tau_{ij}\frac{\partial u_j}{\partial x_j} - \beta \omega^2 + \frac{\partial}{\partial x_j}\left[\left(\nu + \sigma_\omega \nu_t\right)\frac{\partial \omega}{\partial x_j}\right] + 2\left(1 - F_1\right)\frac{\sigma_{\omega 2}}{\omega}\frac{\partial k}{\partial x_j}\frac{\partial \omega}{\partial x_j}. \tag{17}$$

In this formulation, the blending function of the model coefficients (F_1) is equal to one in the inner part of the boundary layer to have Wilcox's k-ω model [60] near solid walls, while in the outer part, near boundary layer edges and in free-shear layers, it decreases to zero in order to obtain the k-ϵ model [60]. The closure coefficients β, β^*, γ, σ_k, and σ_ω are defined by the coefficients of the original k-ω model (ϕ_1) and the transformed k-ϵ model (ϕ_2) as:

$$\phi = F_1\phi_1 + (1 - F_1)\phi_2, \quad \text{where} \quad \phi = \{\beta, \gamma, \sigma_k, \sigma_\omega\}. \tag{18}$$

The blending function F_1 is defined as:

$$F_1 = \tanh\left(\left[\min\left\{\max\left\{\frac{\sqrt{k}}{0.09 d\omega}, \frac{500\mu}{\rho d^2 \omega}\right\}, \frac{4\rho\sigma_{\omega 2} k}{CD_{k\omega} d^2}\right\}\right]^4\right), \tag{19}$$

where $CD_{k\omega}$ stands for the positive portion of the cross-diffusion ($\frac{\partial k}{\partial x_j}\frac{\partial \omega}{\partial x_j}$) in the k-ω model.

For the k-ω SST model proposed by Menter et al. [41], this definition of the turbulent eddy viscosity is modified by using a blending function F_2 which is active in boundary layer flows,

$$\nu_t = \frac{\mu_t}{\rho} = \frac{k/\omega}{\max\left\{1, \Omega F_2/(a_1\omega)\right\}}. \tag{20}$$

Thus, in turbulent boundary layers, the maximum value of the eddy viscosity is limited by forcing the turbulent shear stress to be bounded by the turbulent kinetic energy times $a_1 = 0.31$. This effect is achieved with the absolute value of the vorticity Ω and the blending function F_2, defined as a function of wall distance d:

$$F_2 = \tanh\left(\left[\max\left\{2\frac{\sqrt{k}}{0.09d\omega}, \frac{500\mu}{\rho d^2\omega}\right\}\right]^2\right). \tag{21}$$

The k-ω SST model transport equations are implemented in the LBM solver using finite differences on the Cartesian grid. These transport equations are solved during the collisions step to account for turbulence effects on the flow. Regarding the discretization of these equations, a fourth-order centered scheme is utilized for the derivatives with special treatments for the nodes close to boundaries and grid transitions, where the second neighbor nodes are not available. For the nodes close to the wall, the gradient scheme switches to a one-sided finite difference, and for the nodes close to transitions, the second-order centered scheme is used. For the advection terms, a hybrid TVD centred/upwind scheme is applied. In addition, a modified version of the Van Albada 1 slope limiter [55] is employed in the TVD scheme to avoid high flux rates of ω for the nodes near the wall. This limiter is calibrated on the inclined flat plate case for the k-ω SST turbulence model in the ProLB solver.

One of the advantages of k-ω turbulence models, in the case of a body-fitted mesh, is that the Dirichlet boundary condition can be used for the turbulence model quantities (k and ω) and near-wall values can be resolved by sufficiently refined grids. In ProLB however, as discussed in Section 2.2, the near-wall treatment is also needed for the estimation of the turbulence parameters at the boundary nodes. Thus, a wall function is used for the representation of k and ω in the vicinity of the wall based on the wall distance and the friction velocity, which is computed by the wall model in the viscous sublayer and the log layer, as it is discussed in Section 2.2.

For viscous sublayer where $y^+ < 11.06$ [27]:

$$k_{vis} = C_k u_\tau^2 {y^+}^{3.23} \quad \text{and} \quad \omega_{vis} = \frac{6u_\tau^2}{\nu\beta_1 {y^+}^2}, \tag{22}$$

and in log layer ($y^+ \geq 11.06$):

$$k_{log} = \frac{u_\tau^2}{\sqrt{C_\mu}} \qquad \text{and} \quad \omega_{log} = \frac{u_\tau^2}{\nu\sqrt{C_\mu}\kappa y^+}, \tag{23}$$

where C_k, C_μ and β_1 are the turbulence constant parameters. As it is seen, the extension of each correlation of the viscous layer and log layer is considered as the corresponding value in the buffer layer. Nevertheless, a more accurate representation of ω can be achieved using a blending function [28] as follows:

$$\omega_{log} = \phi\omega_{b2} + (1-\phi)\omega_{b1} \quad \text{where} \quad \phi = \tanh\left(\left(\frac{y^+}{10}\right)^4\right), \tag{24}$$

where ω_{b1} and ω_{b2} are defined based on ω value in Eqs. 22 and 23 as:

$$\omega_{b1} = \omega_{vis} + \omega_{log} \quad \text{and} \quad \omega_{b2} = \left({\omega_{vis}}^{1.2} + {\omega_{log}}^{1.2}\right)^{1/1.2}. \tag{25}$$

In Section 3.1, this k-ω SST turbulence model is validated in a simple 2D turbulent attached flow around an airfoil.

Improved - Delayed Detached Eddy Simulation (IDDES/DDES).

The original version of the DES model [47] is based on a modification of the Spalart-Allmaras (SA) one-equation model [48]. However, its principle can be generalized to all RANS models by an appropriate adjustment in the reference length scale in order to modify the dissipation of the RANS turbulence model ($\beta^*\omega k$ in Eq. 16) [51, 54]. The very first limitation of the DES model corresponded to a certain transition region downstream of the RANS-LES interface which was called the *grey area*. At the RANS-to-LES interface, the modeling is switched instantly from a non-turbulence resolving method to a turbulence-resolving method across a single grid plane. The eddy viscosity is reduced, and therefore the modeled Reynolds stress drops. However, the resolved turbulent stresses associated with the resolved

flow unsteadiness are not instantly fully developed to replace this reduction of the modeled turbulence. Since in the incoming RANS-simulated flow, there are no or only weak natural instabilities, a certain transition region downstream of the RANS-LES interface is needed for the LES-simulated flow to develop resolved turbulence - if it develops at all. The effect of this transition region was detected among the first test cases [50] in which the DES model was used and is referred to as modeled-stress depletion (MSD). The effects of the grey area become much more pronounced if the RANS mode is switched to LES inside the attached boundary layer and in severe cases lead to grid-induced separation (GIS)[42].

They proposed a solution within the SST DES framework, using the two blending functions F_1 and F_2 to identify the boundary layer and prevent a switch to LES inside the boundary layer. Spalart [49] generalized the idea of Menter's proposal, which can be applied to any model as long as the eddy viscosity is involved. This modification is applied by redefining the DES length scale.

Therefore, the dissipation term in the k-equation for the SST DDES model reread as

$$\beta^* \omega k \rightarrow \beta^* \omega k F_{DDES}, \tag{26}$$

where

$$F_{DDES} = \frac{l_{RANS}}{l_{DDES}}. \tag{27}$$

The DDES length scale, l_{DDES}, is defined as

$$l_{DDES} = l_{RANS} - f_d \max\left\{0, (l_{RANS} - l_{LES})\right\}, \tag{28}$$

where the delaying function, f_d, is given by:

$$f_d = 1 - tanh[(C_{d1} r_d)^{C_{d2}}], \tag{29}$$

where $C_{d1} = 20$, $C_{d2} = 3$, and $r_d = \frac{\nu_t + \nu}{\kappa^2 d_w^2 \sqrt{0.5 \cdot (S^2 + \Omega^2)}}$. This delaying function goes to zero in boundary layers, to ensure that DDES performs in its RANS mode in the major part of any attached boundary layer independent of the wall-parallel grid spacing. Here S is the magnitude of the strain rate tensor, Ω is the magnitude of the vorticity tensor, d is the wall distance, and $\kappa = 0.41$. In the case of a rectilinear hexahedral cell, L_{LES} is defined proportional to the maximum edge length of the cell, $L_{LES} = C_{DES} h_{max}$, where $C_{DES} = C_{DES,1} F_1 + C_{DES,2}(1 - F_1)$, with $C_{DES,1} = 0.78$ and $C_{DES,2} = 0.61$.

The Improved Delayed Detached Eddy Simulation (IDDES) model [20, 46] is a hybrid RANS-LES model (consisting of a combination of various new and existing techniques) that provides a more flexible and convenient scale-resolving simulation (SRS) model for high Reynolds number flows. In addition to providing shielding against grid-induced separation, similar to the DDES model, it allows the model to run in Wall-Modeled LES mode in case unsteady inlet conditions are provided to simulate wall boundary layers in unsteady mode.

Similar to DDES, the IDDES-SST model is based on modifying the sink term in the k-equation of the SST model.

$$\beta^* \omega k \rightarrow \beta^* \omega k F_{IDDES}, \tag{30}$$

$$F_{IDDES} = \frac{l_{RANS}}{l_{IDDES}}, \tag{31}$$

where

$$l_{IDDES} = \hat{f}_d \cdot (1 + f_e) \cdot l_{RANS} + (1 - \hat{f}_d) \cdot l_{LES}. \tag{32}$$

The $\hat{f}_d$ is an empirical blending function that combines the two branches DDES and WMLES. The elevating function f_e is also defined to prevent the excessive reduction of the RANS Reynolds stresses in the vicinity of the RANS and LES interface and to ensure that the log-layer mismatch does not occur. A detailed description of these functions can be found in [20].

Continuous eddy simulation (CES).

In the Continuous Eddy Simulation [22], it was tried to tackle the most significant issue of hybrid RANS/LES turbulence models in properly balancing the contributions of resolved and modeled motions. In hybrid RANS/LES turbulence models, grids determine resolved motion (fluctuations), and the model produces modeled motion in response to the inability of the grid to fully resolve. Regarding this, under the wide grid and Reynolds number variations, this theory-based method can properly detect and respond to the actual flow resolution by adjusting the modeled viscosity to the degree of flow resolution such that the total motion is kept in balance. This opens the way to successfully address the lack of control of modeled and resolved motions that are involved in hybrid simulations.

The hybridization of the k-ω SST RANS equation is accomplished by a modification of the dissipation term in the k equation in correspondence to the DES version of k-ω SST model [24].

$$\beta^* \omega k \rightarrow \beta^* \omega k \psi_\beta, \tag{33}$$

where $\psi_\beta = \beta + R(1-\beta)$ and R is a model parameter $R = L_+^2$.

The proper information about the amount of resolved motion produced on the applied grid is transferred to the model via a resolution indicator of L_+. L_+ is the turbulence length scale resolution ratio which involved the modeled contribution L and the total (RANS) length scale L_{tot} (for the k-ω SST model $L_{tot} = \sqrt{k}/(C_\mu \omega)$). This parameter can be related to the filter width Δ [23]:

$$L_+ = \frac{\Delta_{C+}}{(1+\Delta_{C+}^3)^{1/3}}, \tag{34}$$

where $\Delta_{C+} = C_+ \Delta_+$ with constant parameter C_+ and $\Delta_+ = \Delta / L_{tot}$.

3. Results and discussion

The k-ω SST RANS turbulence model described above and its derived hybrid RANS/LES models are implemented in the ProLB solver. A 2D airfoil test case is selected to validate and check the behavior of the k-ω SST RANS model in comparison with the already validated SA model. To evaluate the capability of the hybrid RANS/LES models for predicting the flow in fully turbulent attached and separated boundaries, the three-dimensionality of turbulence should be taken into account. Therefore, a fully turbulent 3D airfoil case in large angles of attack is considered. A generic vehicle model, the Ahmed body case, is included as well, to demonstrate the improvements in accuracy due to the application of hybrid RANS/LES models for the separation and reattachment regions, relative to the RANS simulations.

3.1. 2D NACA-23012 airfoil

The first test case is a NACA-23012 airfoil (Fig. 2a) with a chord (c) of 0.46 m ($18in$) and a span (s) of $8\%c$. The airfoil at several angles of attack ($\alpha = 0°$, 6.2° and 9.3°) exposes to a flow with $Ma = 0.18$ which is associated to a chord-based Reynolds number $Re_c = 1.88 \times 10^6$. For the LBM simulation, the speed of sound is $C_s = 340\ m/s$ and the kinematic viscosity is $\nu = 1.5 \times 10^{-5}\ m^2/s$. The computational domain is chosen in a way that the distance between the inlet and the airfoil is 10 times the chord length ($x/c = -10$) and the outlet is located at $x/c = 20$. In the Y direction, the top and bottom boundaries are at $y/c = \pm 10$.

Regarding the boundary conditions, the free-stream velocity is imposed at the inlet and the bottom boundaries with an angle corresponding to the angle of attack. For the outlet and top boundaries, the constant density condition is applied.

Moreover, a fixed velocity and a fixed density sponge layers [64] are also defined at the inlet and outlet boundaries, respectively, to ensure convergence toward a steady state and prevent spurious reflection of disturbances.

A multi-tree formulation is used to refine the grid around the airfoil. The domain primarily consists of $345 \times 230 \times 1$ cells in streamwise, vertical, and spanwise directions.

The cell size at the coarsest level is equal to 8.7%c ($\Delta_{max} = 0.04$ m), which corresponds to the domain size in the spanwise direction (z). The D3Q19 lattice velocity model can still be employed for this simulation due to the thin domain's width in the spanwise direction. Periodic boundary conditions are therefore implemented in this direction. Using isotropic refinement, the grid size is halved at each refinement level with two refinement types: rectangular boxes and offsets from the airfoil surface (Fig. 2b). The final mesh consists of 3.8×10^6 nodes after 6

levels of refinement steps ($n = 6$), namely 3 refinement boxes and 3 refinement offsets, with the minimum grid size of $\Delta_{min} = \frac{8.7\%c}{2^n} = 0.000625$ m.

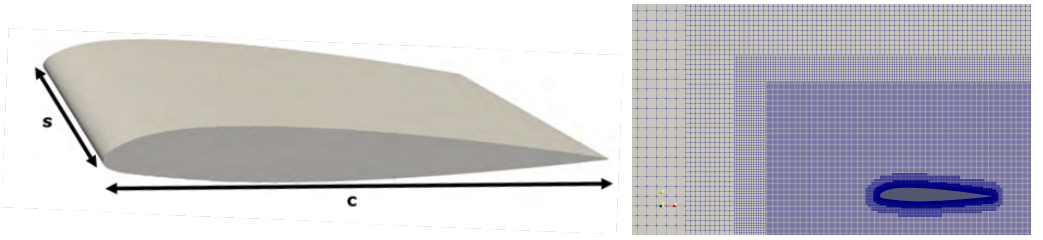

(a) NACA-23012 (b) Refinement levels

Figure 2: The geometry (a) and the mesh resolution (b) around the NACA-23012 airfoil.

The computations are performed up to 200,000 timesteps which correspond to over 15 flow-through-time (c/U_∞) to ensure the convergence toward a steady state. The evolution of the aerodynamic forces (lift F_y and drag F_x) in Fig. 3 confirms that the convergence is obtained after around 100,000 timesteps for all the computations.

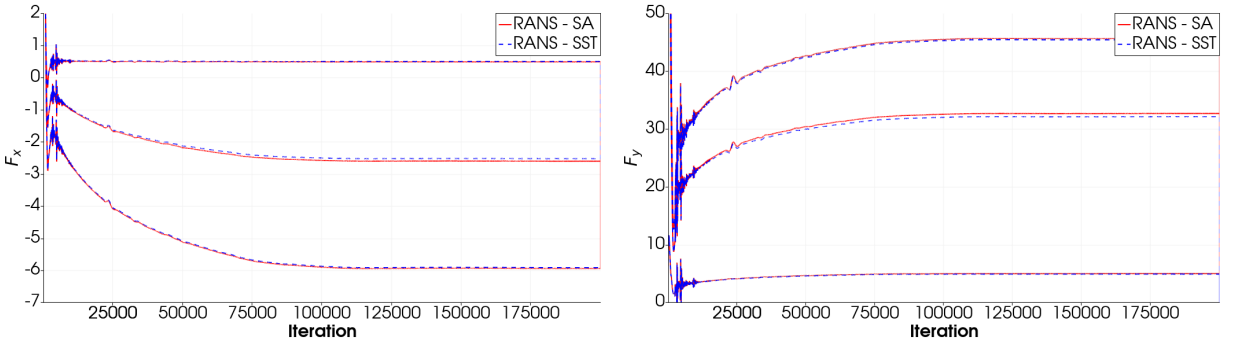

(a) F_x (b) F_y

Figure 3: The convergence of lift (F_y) and drag (F_x) forces during the computational time.

The activity of the turbulence model can be analyzed in light of the turbulent kinetic viscosity (ν_t). The turbulent kinetic viscosity is the parameter used for computing the relaxation time in Eq. 6 in LBM. It is actually a link between the turbulence modeling part and the rest of the ProLB solver (see Section 2.1). The averaged turbulent kinetic viscosity for the k-ω SST and the SA turbulence models are presented in Fig. 4. The solutions of the two turbulence models are very close except for the angle of attack $\alpha = 0°$ where the level of the turbulent viscosity for the simulation with the k-ω SST model is lower than the SA model (Fig. 4a).

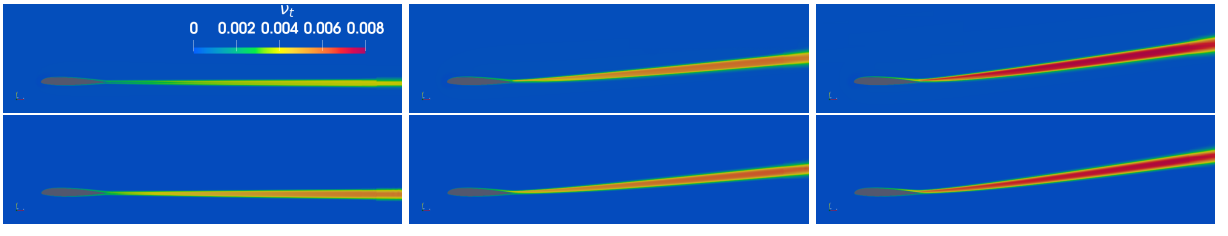

(a) $\alpha = 0°$ (b) $\alpha = 6.2°$ (c) $\alpha = 9.3°$

Figure 4: The distribution of the turbulent kinetic viscosity (ν_t) in the wake of the airfoil for k-ω SST (top) and SA (bottom).

The turbulent kinetic viscosity level at several locations of the wake (Fig. 5) also confirms that as the angle of attack increases, the production of the turbulence in k-ω SST is large enough to compensate for the differences with SA. In the wake of the k-ω SST simulation at $\alpha = 0°$, there is a symmetry between the flow coming from the suction side of the airfoil and the flow which passed the pressure side. At higher angles of attack, this symmetry disappears in favor of the suction side.

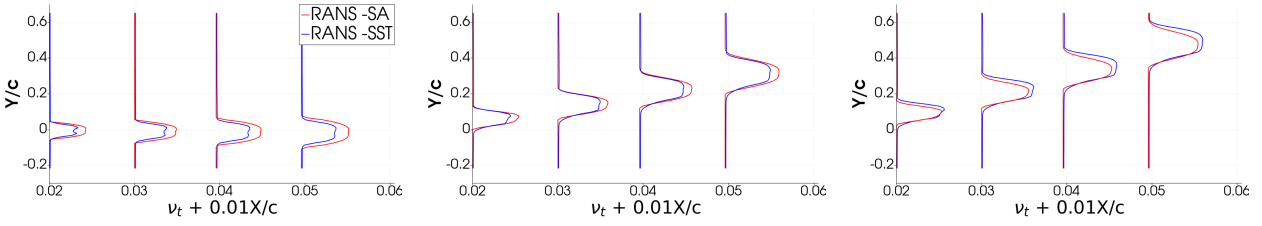

(a) $\alpha = 0°$ (b) $\alpha = 6.2°$ (c) $\alpha = 9.3°$

Figure 5: The distribution of turbulent kinetic viscosity in the wake of the airfoil at locations X/c = 1, 2, 3 and 4; blue line: k-ω SST, red line: SA.

The aerodynamic performance of an airfoil is classically evaluated using the lift (C_L) and drag (C_D) coefficients. These coefficients can be calculated by the surface integration of the pressure and viscous forces applied to the airfoil. However, as also discussed by Wilhelm et al.[62], for Cartesian (non-body-fitted) grids, since the pressure and stress tensor are calculated at the boundary nodes which do not systematically lie on the airfoil surface, these quantities have to be extrapolated on the vertices of the surface grid of the airfoil to perform the integration. They discussed that the forces acting on a body can also be obtained with far-field integration. In that case, these forces are derived from the global conservation law of momentum applied to a control volume encompassing the body. In this study, the same approach is considered and the lift and drag coefficients are obtained by far-field integration using a defined control volume around the airfoil for the three angles of attack. The comparison of these coefficients with the experimental data [4] is presented in Table 1.

Table 1
Lift and drag coefficient of NACA-23012 at angles of attack $\alpha = 0°$, 6.2° and 9.3° for SA, k-ω SST and experiments [4].

Angle of attack (α)	C_L			C_D		
	RANS-SST	RANS-SA	Exp.	RANS-SST	RANS-SA	Exp.
0°	0.12	0.12	0.12	0.0074	0.0081	0.0075
6.2°	0.83	0.79	0.79	0.0081	0.0083	0.009
9.3°	1.12	1.175	1.07	0.014	0.012	0.0125

The predicted lift coefficient, regardless of the choice of the turbulence model, is very close to the experimental data. For the drag coefficient however, by increasing the angle of attack, the difference between the predicted value and the reference data increases. This discrepancy at the angle of attack 9.3° is even wider, particularly for the k-ω SST model. This proximity in the solutions of the k-ω SST and SA models is also observed for the prediction of the mean pressure coefficient (C_p) and skin friction coefficient (C_f) on the surface of the airfoil (Fig. 6 and 7).

The predicted pressure coefficient, for both the turbulence models, is under-estimated in comparison with the data reported by Lee et al. [32] for $\alpha = 0°$ and Broeren et al. [4] for $\alpha = 6.2°$ and 9.3°. Around the leading edge, the underestimation of the predicted solution is more profound. This may be due to the inability of the RANS models in simulating local transitional flow in the starting part of the boundary layer.

There is also a disagreement between the predicted skin friction coefficient of both turbulent simulations around the leading edge of the airfoil and the reference data from the Xfoil predictions [16] and a body-fitted simulation using the elsA software [9] with wall resolved grid ($y^+ < 1$ near the wall).

Using a mesh with a higher resolution around the leading edge of the airfoil, the discrepancies between the simulation solutions and the reference data are reduced. In Fig. 8, it is seen that for the angle of attack 9.3°, the error

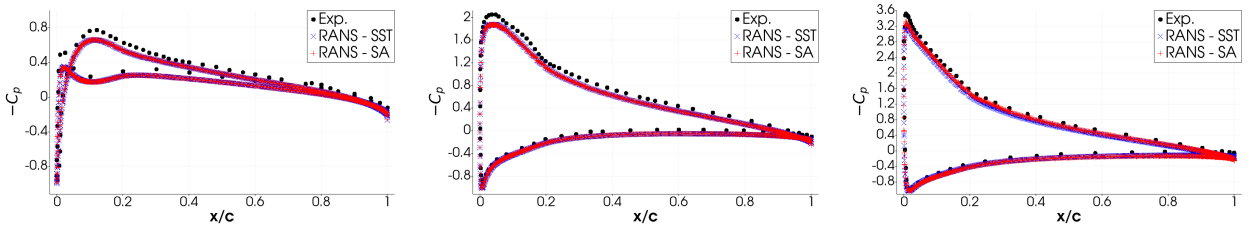

(a) $\alpha = 0°$ (b) $\alpha = 6.2°$ (c) $\alpha = 9.3°$

Figure 6: The distribution of mean pressure coefficient (C_p) along the airfoil; blue line: k-ω SST, red line: SA, black point: experimental data [4, 32].

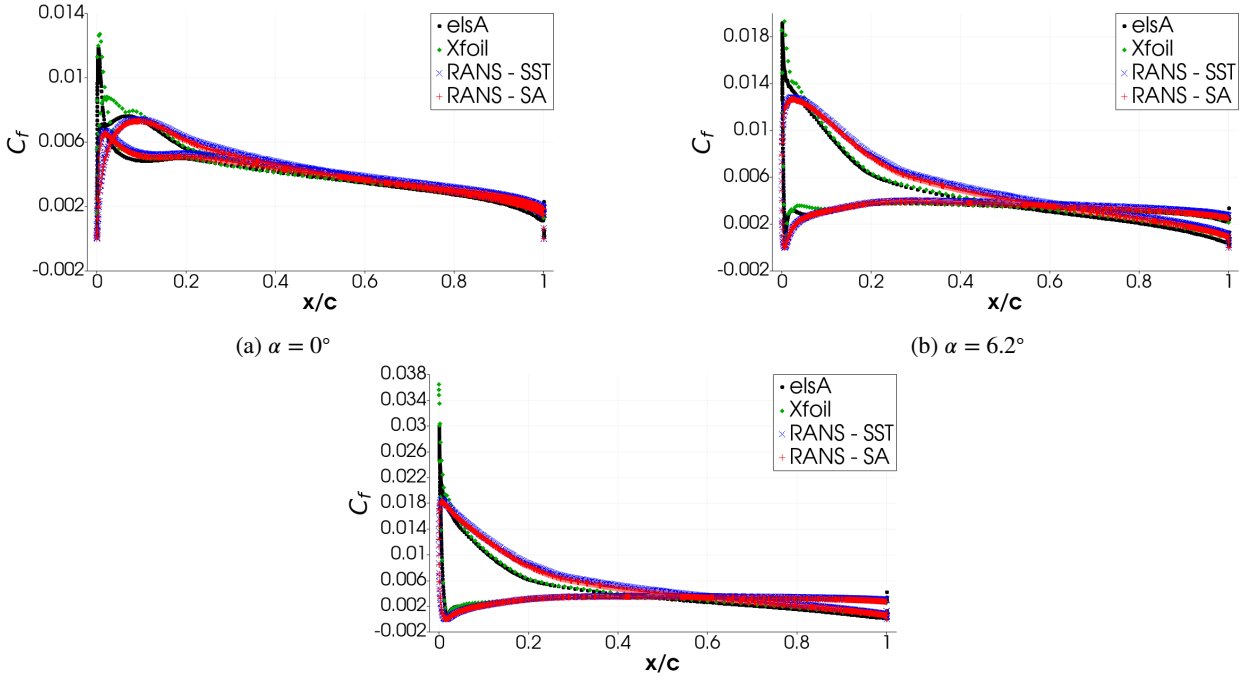

(a) $\alpha = 0°$ (b) $\alpha = 6.2°$

(c) $\alpha = 9.3°$

Figure 7: The comparison of the mean friction coefficient (C_f) along the airfoil with reference data.

is reduced by almost 50% after applying one more level of refinement (one step halving the local grids) only at the leading edge. There are also improvements in predicting the skin friction coefficient by applying a higher local mesh resolution around the leading edge. Nevertheless, the differences with the reference data are still significant.

3.2. 3D NACA-0012 airfoil

In order to validate the hybrid RANS/LES turbulence models the 3D effect of turbulence should be taken into account. Therefore, as the second test case with the same near-wall treatment, a NACA-0012 airfoil is considered with an aspect ratio equal to the chord length of the airfoil. The computational domain in the X and Y directions is a bit larger than in the previous test case. The inlet is located at $x/c = -30$, with the outlet at 60 times of the chord length ($x/c = 60$) behind the airfoil. Also in the Y direction, the top and bottom boundaries are at $y/c = \pm 30$.

The boundary conditions are kept the same as before: the free-stream velocity is imposed at the inlet and the bottom boundaries with an angle corresponding to the angle of attack, the constant density condition for the outlet and top boundaries, and the periodic boundary condition in the spanwise direction. In addition, the probable spurious reflection of disturbances is prevented using sponge layers at the inlet and outlet boundaries.

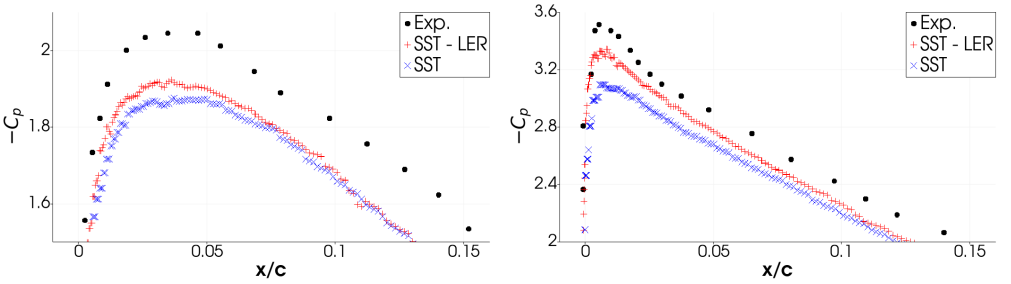

(a) $\alpha = 6.2°$ (b) $\alpha = 9.3°$

Figure 8: The distribution of mean pressure coefficient (C_p) along the airfoil for k-ω SST model on: the original mesh (blue), the original mesh with an extra level of leading-edge refinement (red). black point: experimental data [4, 32].

For this study, the airfoil exposes to a turbulent flow with the associated Reynolds number of $Re_c = 3 \times 10^6$ based on the chord length at several angles of attack. First, the angles of attack of $\alpha = 2°, 6°, 10°$ and $15°$ are considered at which there is a fully attached boundary layer around the airfoil. The flow is also studied around the airfoil at a high angle of attack (e.g. $\alpha = 45°$ or $60°$), where aerodynamic characteristics of the airfoil are changed due to the forced stall condition.

Regarding the mesh generation, the far-field coarse grids with a maximum grid spacing $\Delta_{max} = 0.226\,\text{m}$ are refined gradually to the near-wall region with the local cell size of $\Delta_{min} = 0.00176\,\text{m}$ ($\approx 0.18\%c$). This isotropic refinement process is applied through 7 levels of refinement consisting of 3 refinement boxes, 3 refinement offsets around the airfoil body, and one excessive level of treatment at the leading and trailing edges (Fig. 9).

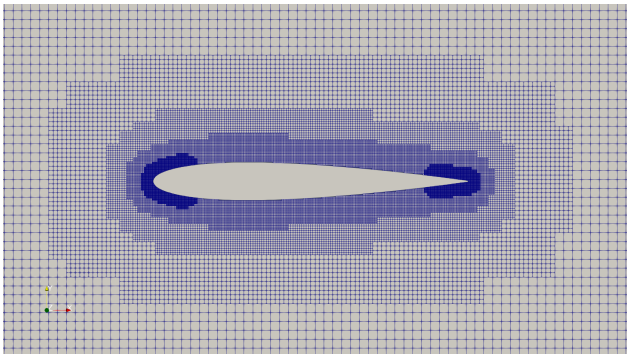

Figure 9: The mesh resolution around the NACA-0012 airfoil.

The computations continue for a sufficiently long time corresponding to over 80 flow-through-time, and the converged solutions are obtained by averaging over the 27 flow-through-time.

Regarding the simulations with low angles of attack ($\alpha = 10°, 15°$), the hybrid RANS/LES models behave more or less the same as the RANS computations. The mean pressure coefficient distribution in IDDES, CES, and RANS simulations are identical for the airfoil at $\alpha = 10°$ (Fig. 10). For $\alpha = 15°$, a slight impact of the hybrid models is observed on the suction side of the airfoil after the leading edge. This can be the effect of the attempts of the hybrid models in resolving the local transition boundary layer. According to Fig. 11, the local grid resolution around the leading edge allows the models to behave as LES even inside the thin boundary layer (the outer region) and only a few first-off body nodes are treated with RANS. Therefore, this may cause an increase in the prediction of turbulence in this region. It is obvious that after the grid transition interface, the grids are not fine enough to permit LES to be activated inside the boundary region, so the near-wall solutions tend towards pure RANS computation. Afterward, in Fig. 10b, a small drop at $x/c = 0.15$ is related to the local grid transition of the leading edge treatment.

It is good to mention here that one of the differences between the IDDES and CES hybrid models corresponds to the transition region between RANS and LES (Fig. 11). In IDDES simulations this transition is relatively thin. However

for CES, as the name implies (continuous eddy simulation), there is a smooth transition from RANS computations for the near-wall nodes to the LES region.

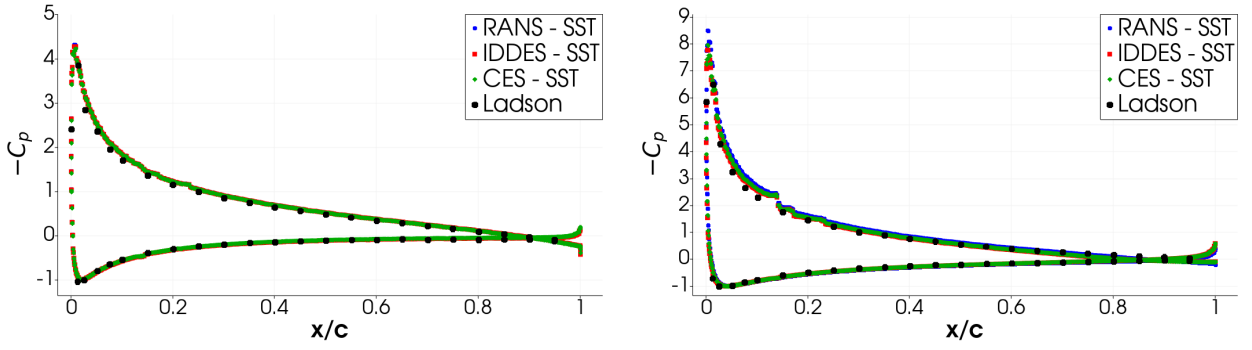

(a) $\alpha = 10°$ (b) $\alpha = 15°$

Figure 10: The distribution of mean pressure coefficient (C_p) along the NACA-0012 airfoil for: the k-ω SST RANS (blue circle), IDDES (red square), and CES (green diamond) models compared with the experimental data by Ladson [31] (black point).

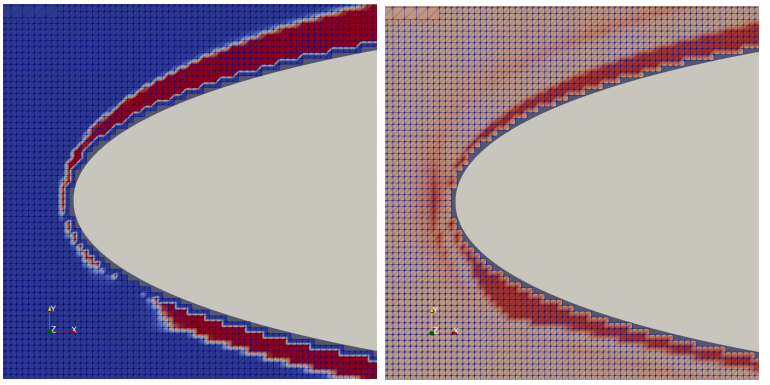

(a) $\hat{f}_d$ in IDDES (b) ψ_β in CES

Figure 11: Change in the behavior of the hybrid models around the body from RANS (dark red) in the near-wall region to LES for the far-field flow. The color bar for ψ_β has been manipulated to have a better representation of RANS region.

The aerodynamic forces for these simulations are compared with the reported experimental data by Ladson [30] in Fig. 12. As discussed before, far-field integration over a control volume around the airfoil is used to compute the forces acting on the body. The predicted lift (C_L) and drag (C_D) coefficients for $\alpha = 2°$, $6°$, and $10°$, regardless of the choice of turbulence model, are close to the reference data. At $\alpha = 15°$ however, a slight discrepancy is observed for the predicted value of the RANS simulation. One of the sources of larger differences with the experimental data with the hybrid RANS/LES models is due to larger unsteadiness in the solutions which affects the averaged solution. Therefore, a longer computational time with a larger averaging interval is needed to obtain a fully converged solution. However, as the angle of attack increases, the boundary layer gets closer to detachment and the flow becomes unsteady. Therefore, the effect of flow unsteadiness on the mean solution will be even greater.

Another source of the error corresponds to applying an equilibrium wall model as a near-wall treatment for the boundary layer which is subject to high adverse pressure and flow separation. The impact of applying an equilibrium wall model for a boundary layer under adverse pressure gradients is discussed later in Section 3.3.

To study the performance of hybrid models, the simulation of the airfoil at $\alpha = 45°$, for which the RANS turbulence model is no longer efficient due to the presence of a fully detached boundary layer and highly unsteady flow, is tested. Figure 13 represented the turbulent structure of the flow for the simulations using RANS, IDDES, and CES turbulence

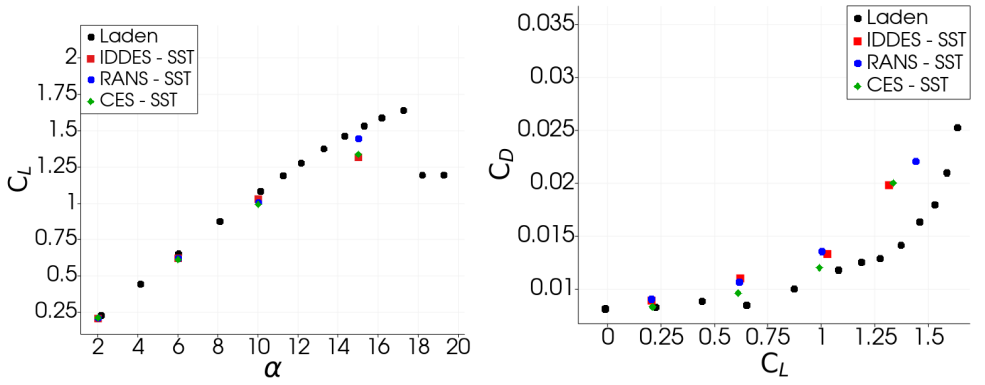

Figure 12: Lift C_L and Drag C_D Coefficients. k-ω SST RANS (blue circle), IDDES (red square), and CES (green diamond) models compared with the experimental data by Ladson [30] (black point).

models. As it is seen, more turbulent small structures are captured when the hybrid RANS/LES models are used. This leads to higher unsteadiness in the solutions. Therefore, as mentioned above, the averaging interval needs to be increased to obtain a converged solution. For this specific case, in order to achieve a converged aerodynamics coefficient regardless of the location of the integrating control volume (see Section 3.1 and [62]), the computational time increases to 234 flow-through-time, and the averaging interval is equal to 110 flow-through-time over the airfoil.

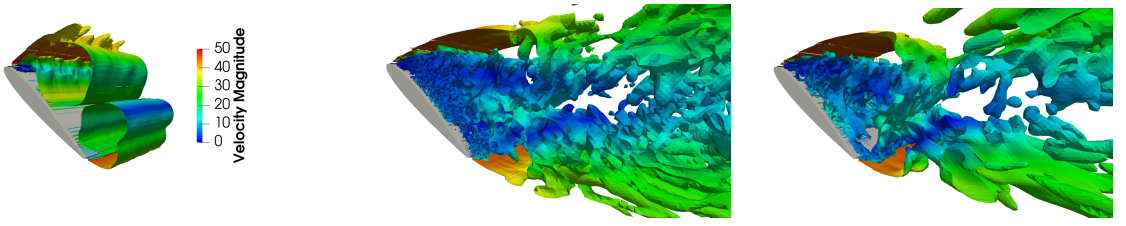

(a) $RANS$ (b) $IDDES$ (c) CES

Figure 13: The iso-surface Q criterion ($Q = 50$) over the Naca-0012 airfoil at 45° angle of attack (colored by the velocity magnitude).

As presented in Table 2, the averaged predicted values of the lift and drag coefficients for the hybrid RANS/LES turbulence models are in agreement with reference data, contrary to the RANS simulation.

Table 2
Lift and drag coefficient of NACA-0012 at angles of attack $\alpha = 45°$, comparing with reference data by [45].

Angle of attack (α)		RANS	IDDES-SST	CES-SST	Exp.
45°	C_L	2.238	1.231	1.192	1.097
	C_D	2.053	1.038	0.993	1.180

For low angles of attack, the hybrid RANS/LES turbulence models behave as a RANS simulation which performs well for this attached boundary flow. In a large angle of attack however, the generation of the small turbulent structure in the vicinity of the body is enough to activate the limiter functions and the model behaves as LES in this region. In comparison to fully RANS simulations, the hybrid RANS/LES turbulence models significantly improve the ability to capture flow features and estimate aerodynamic forces. In this test case, the performance of the IDDES and CES is almost the same without any superiority. Considering all of the above discussions, the hybrid RANS/LES turbulence models based on k-ω SST can be an alternative for the wall-modeled LES in the LBM framework for simulating turbulent flow around complex geometries. Boundary layers are treated by the computationally efficient k-ω SST RANS model, especially in the case of the attached boundary layer where the k-ω SST RANS is applied reliably with

sufficient accuracy to cover the whole boundary region. The hybrid model only exhibits WMLES behavior when a separation occurs.

3.3. Ahmed body

The third test case in this study is an Ahmed body model with a slant surface. This model, as a simplified car model, is a popular model to evaluate the performance of turbulence models in simulating near-wall flows in fully turbulent attached and separated boundaries. The model, as presented in Fig. 14, has the size of 1044×389×288 mm in length (L), width (W), and height (H), with a slant angle of ϕ.

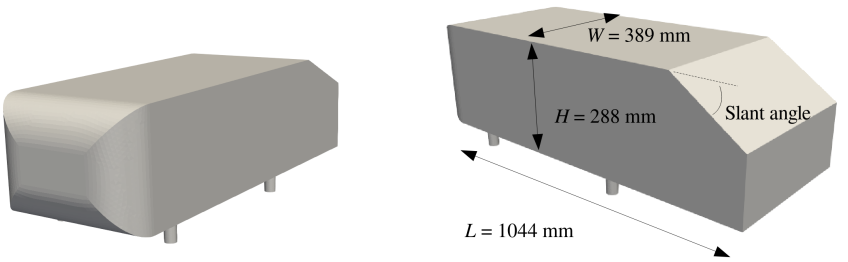

Figure 14: The geometry of the Ahmed body.

This study is mainly focused on the flow structures on the slant surface and in the wake of the body. The flow structures over the Ahmed body are highly three-dimensional and according to the experimental observations, the flow in those regions is highly influenced by the change of the slant angle. At small angles, three major coherent structures can be identified in the wake: (1) a separation bubble in the initial part of the slant followed by a reattachment on the slant surfaces, (2) counter-rotating longitudinal vortices which are generated from the slant side edges, (3) two recirculation bubbles after the vertical base [34]. Above the slant angle $\phi = 30°$, the critical angle at which the maximum drag is obtained, a fully detached flow is observed on the slant surface due to the strong adverse pressure gradient between the slant and the top of the body [34]. Other studies [21, 35, 67] on this geometry also confirmed the evolution of the unsteady flow structures in exchange for a change in slant angles. In this study, to evaluate the ability of the ProLB solver in conjunction with hybrid turbulence models in detecting the described flow evolution, two slant angles of $\phi = 25°$ and $35°$ are considered.

The flow Reynolds number, based on the height of the body (H) and the stream velocity of $U_\infty = 40$ m/s, is $Re_H = 7.68 \times 10^5$, conforming with the experiments conducted by Lienhart and Becker [34]. The computational domain is also determined based on the length of the body (L) as $8L \times 2L \times 1.35L$, according to the ERCOFTAC benchmark test [18] to study the flow and turbulence structures in the wake of Ahmed body with two slant angles of 25° and 35°. The inlet with imposed uniform stream velocity is located at the distance of $2L$ upstream of the leading surface of the body. For the outlet boundary at $5L$ after the model, a fixed density value is applied. In the spanwise directions, the symmetry boundary condition is considered. For the floor where the body model is located, instead of a no-slip condition, a fully explicit wall model is used to represent the near-wall flow characteristic. This wall model is developed by Cai et al. [8] and tested on the ProLB solver (see Section 2.2). For the body surface, besides the use of the explicit wall model for modeling the flow around the Ahmed body, the no-slip boundary condition is also tested. Although the local grids in the vicinity of the body are not sufficiently fine to resolve the turbulence near the wall ($y^+ \gg 1$), the no-slip boundary condition is imposed on the surface of the body. This highlights the impact of the near-wall treatment on the behavior of the flow features near the wall and inside the boundary layer, particularly when a slight detachment happens.

Regarding the meshing process and grid resolution, same as the previous test cases, isotropic refinement is used with several refinement levels around the body model and close to the floor. The final mesh consists of 7 refinement levels and is halved at each level and gradually refined from relatively large cells with $\Delta x_{max} = 166.67mm \simeq 16\%L$ to small grid size ($\Delta x_{min} = 1.3mm$) around the body and in the wake (Fig. 15). The total number of nodes in the final mesh is increased to 45.8×10^6, and the mesh is kept the same for the two cases with 25° and 35° slant angles.

For the Ahmed body with 25° and 35° slant angles, IDDES and CES simulations were done using the fully explicit wall model around the body as well as a no-slip boundary condition for the surface of the body. All the simulations

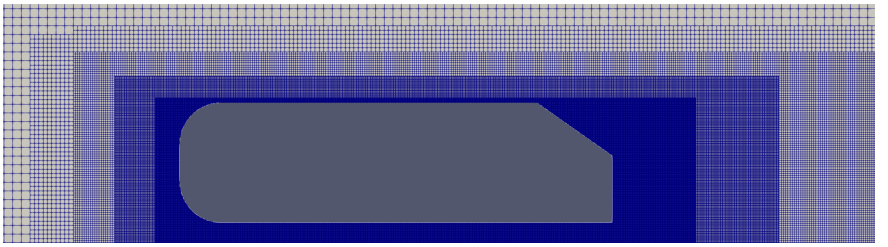

Figure 15: The mesh resolution and refinement levels around the Ahmed body.

for this test case lasted over 100 flow-through-time H/U_∞, and the reported solutions are averaged over the last 50 flow-through-time.

Simulation with a wall model

When the wall model is activated on the body surfaces, regardless of the applied turbulence model, no separation is captured on the slant even for the case with the slant angle 35°. On the contrary, a fully detached boundary layer on the slant surface is observed in the reference data. In Fig. 16, the streamwise velocity around the body of the hybrid simulations is presented for the slant angle 35°. In the simulations with 25° slant angle also, the boundary layer on the slant, under the influence of the wall model, remains attached. Therefore, the solutions of the 25° slant angle with the wall model are not presented.

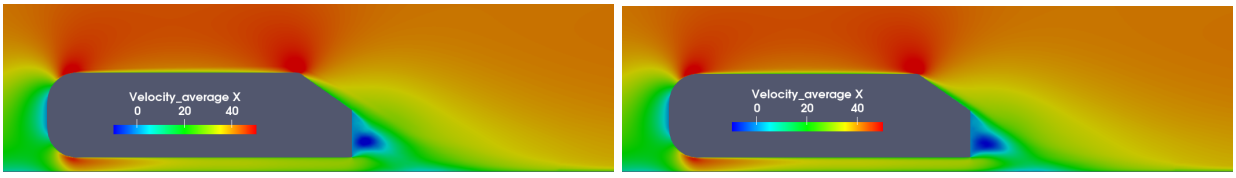

(a) IDDES (b) CES

Figure 16: Averaged streamwise velocity around Ahmed body ($\phi = 35°$) for the hybrid Simulations with wall model condition on the body surface.

As seen before for the airfoil case (Section 3.1), using an equilibrium wall model for a boundary layer under a high adverse pressure gradient can have negative effects on the prediction of surface forces. In addition, in the case of low and mild adverse pressure gradients, the separation can be delayed or may not even happen. The absence of instability in the local solutions on the slant, which prevents the prerequisites for switching from RANS to LES from being met, can be the cause of this behavior. For this test case, the flow characteristic on the slant is completely influenced by the presence of the wall model, and the boundary layer on the slant remains fully attached. In the following, the simulations are repeated without applying the wall model. The tangential velocity vector on the first off-body nodes is linearly interpolated from the no-slip boundary condition on the surface of the Ahmed body and the computed quantities at the reference points (Fig. 1).

Simulation with Dirichlet boundary condition

Contrary to the previous case, by removing the wall model and applying the zero-velocity Dirichlet boundary condition on the body surface, a boundary detachment is observed on the slant (Fig. 17). Regarding the CES simulations, a detachment happens on the top of the body. The detached boundary layer extends to the wake of the body (see Fig. 17b). This behavior is seen for both simulations with slant angles of $\phi = 25°$ and 35°.

For the IDDES simulation of the 35° case with Dirichlet velocity, however, small separation bubbles are observed on the top and the spanwise sides of the Ahmed body, which were not seen in the same simulations with the wall model. Contrary to the CES simulation, the separations reattach to the body surface, though their effects remain until the slant. These effects, which can be seen in the velocity profile along the Ahmed body, are discussed later.

In terms of overall fluid behavior in the wake, despite insufficient local mesh resolution to resolve the near-wall boundary on the slant, the topology of the flow in the wake for the IDDES simulation is in agreement with the reference

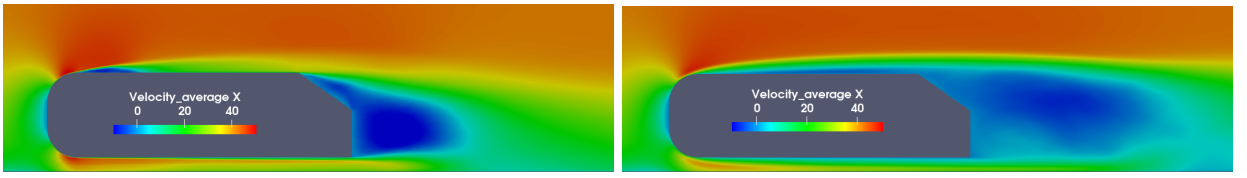

(a) IDDES (b) CES

Figure 17: Averaged streamwise velocity around Ahmed body ($\phi = 35°$) for the hybrid Simulations with Dirichlet boundary condition on the body surface.

data. The comparison of the flow streamlines in the wake of the body is also presented in Fig. 18 for the slant angle 35°. In addition to the two large recirculations in the wake, a small recirculation is also captured near the ending part of the slant which was also reported by the Guilmineau et al. [21] in their IDDES simulation on a body-fitted grid. Regarding the length of the wake, for the IDDES simulations, the wake is a bit larger than the reference simulation and experimental data.

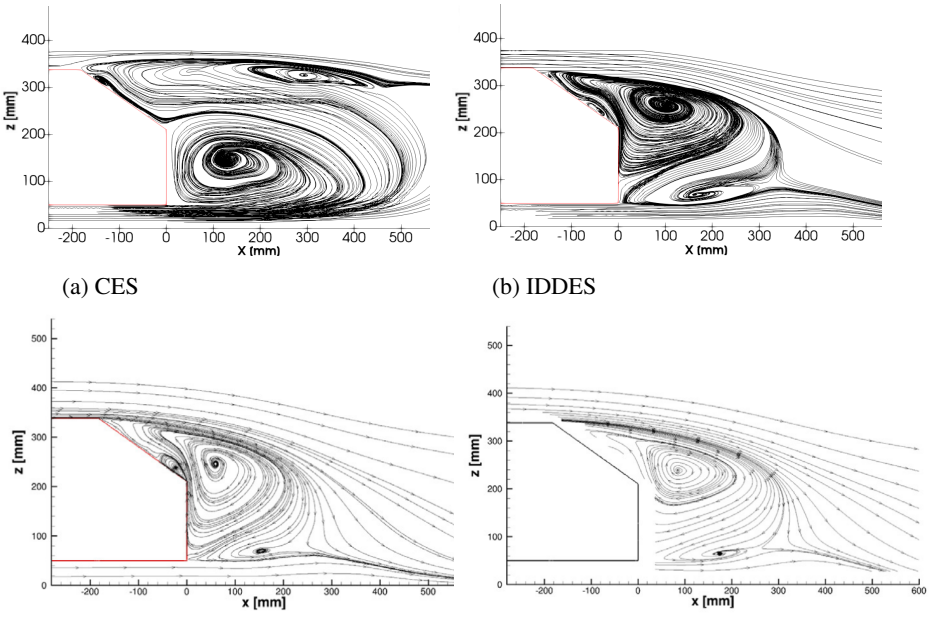

(a) CES (b) IDDES

(c) reference IDDES [21] (d) Exp. [34]

Figure 18: Streamlines in the wake of the Ahmed body with 35° slant angle. The reference figures (c,d) were copied from [21] by permission.

Another description of the wake is presented in Fig. 19, which shows isocontours of streamwise velocity in successive YZ-planes in the wake of the body with CES and IDDES using Dirichlet boundary condition. It is evident that the massive separation on the slant extends beyond the symmetry plane, and the region with negative streamwise velocity spans the entire width of the model. This region continues far into the wake, and remains observable at $X = 500$ mm, especially when using the CES turbulence models. With the IDDES models, the recirculation region extends just over 200 mm, similar to experimental observations. It is important to note that the velocity profile of the boundary layer in the farfield and near the floor is influenced by the local coarse grids. Consequently, one should not expect an accurate representation of the velocity profile in these areas.

To examine in more detail the effects of using a wall model or zero-Dirichlet boundary condition for the body, the streamwise velocity and u_{rms} profiles on the slant and in the wake of the body are presented in Figs. 20 and 21 for the slant angle 35°. It can be seen that the flows in front and on top of the Ahmed body are well predicted for the simulations with the wall model applied to the body, while the differences become apparent on the slant surface and

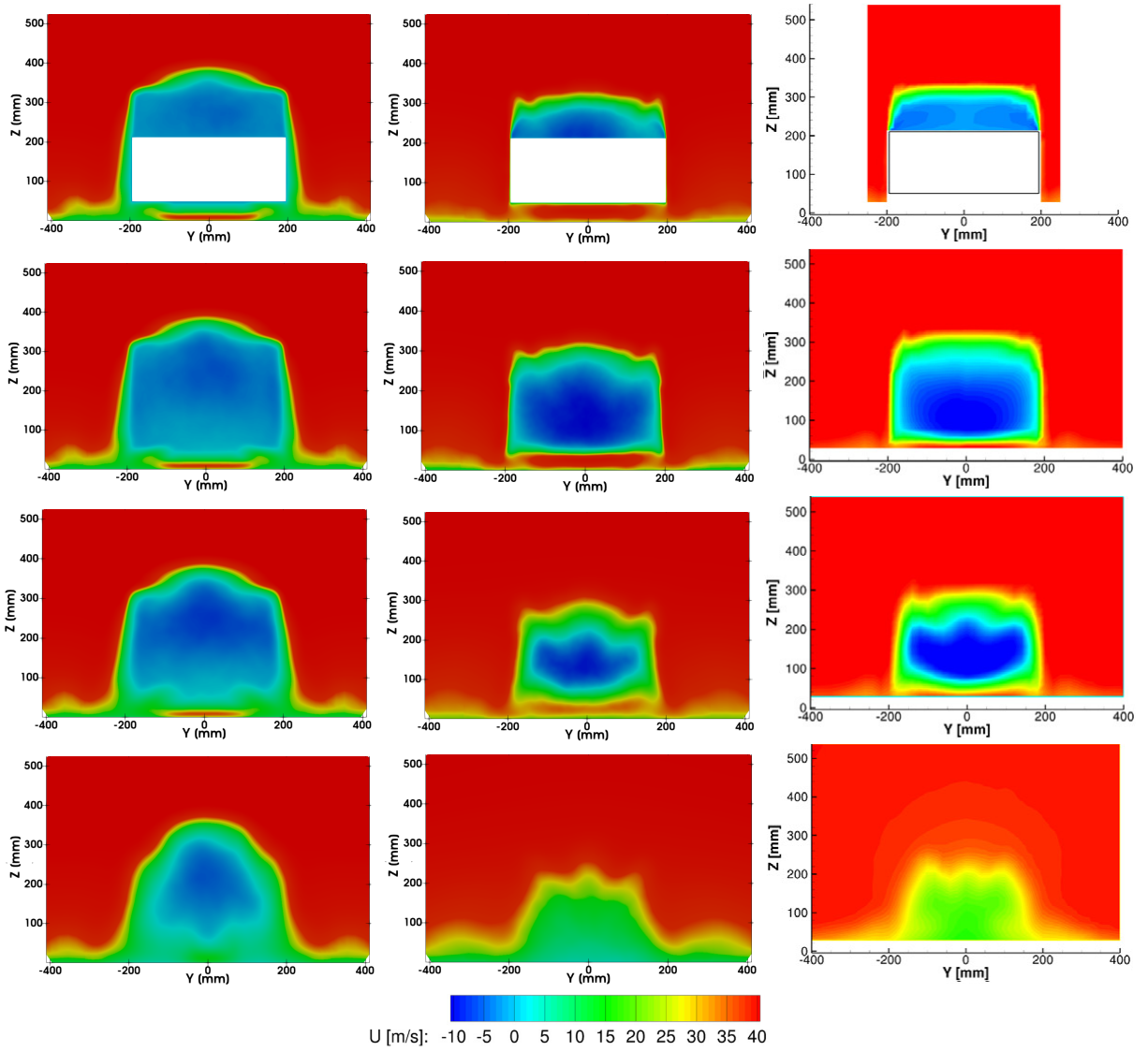

Figure 19: Averaged streamwise velocity in successive YZ-planes in the wake of the Ahmed body with a 35° slant angle. Columns represent CES (Left), IDDES (Center), and reference experiment (Right). Rows correspond to X-locations of 0 mm, 80 mm, 200 mm, and 500 mm, from top to bottom. The experiment figures were copied from [21] by permission.

in the wake. The nonphysical attachment on the slant leads to wrong velocity prediction and turbulent content in this region (Fig. 21). Removing the wall model and applying a zero-velocity Dirichlet boundary condition, in addition to a separation on the slant, causes separations on the top of the Ahmed body and the two sides of the body (not shown here) in both IDDES and CES simulations. As discussed before, these separations for CES slide all the way to the wake of the body and change the velocity profiles in opposition to the reference data. In the IDDES simulation, despite the reattachment of these small separations, their effects on the predicted velocity profiles on the top of the Ahmed body are evident (Fig. 20). This incompatibility in the solutions gradually decreases after the reattachment, although it does not completely disappear until the initial parts of the slant.

The WMLES in the LBM framework was tested in the Ahmed body with a slant angle of 35° test case in the same simulation condition (see [6]). Regarding the mean velocity profiles on the slant and aerodynamic forces, the IDDES turbulence model with the Dirichlet boundary condition for the Ahmed body could recover the WMLES solution. Comparatively to the WMLES simulation, the application of this hybrid turbulence model has a non-negligible impact on the computing speed by replacing WMLES with a less expensive RANS model in areas where this model can be

employed with high reliability and accuracy (e.g. attached boundary layer on top and around the Ahmed body). On the slant, the RANS switches to LES, and the near-wall region is resolved. However, as discussed above, since the applied wall model was developed based on the data of boundary layers at equilibrium and the impact of the adverse pressure gradient is not taken into account, the fully attached boundary layer is predicted as the hybrid model treats as RANS.

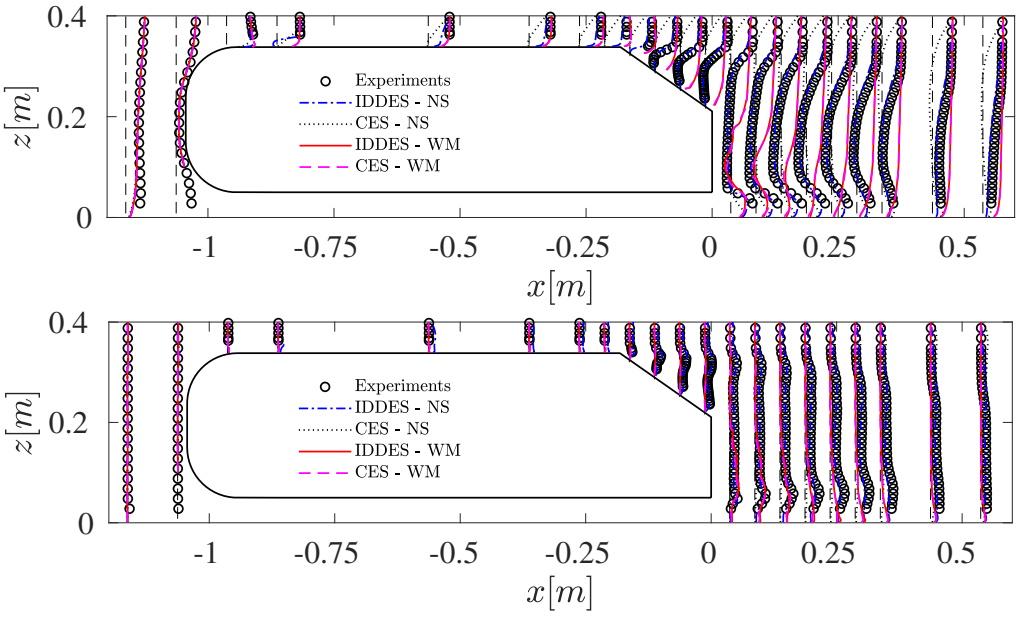

Figure 20: Comparison of the mean streamwise velocity (top) and u_{rms} (bottom) for the flow over the Ahmed body with 35° slant using a wall model (WM) or zero-velocity Dirichlet boundary condition (NS).

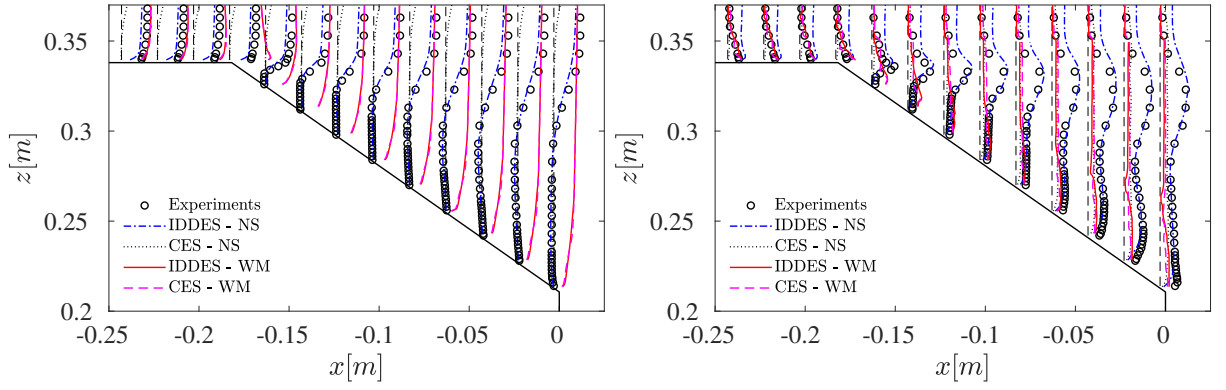

Figure 21: Comparison of the mean streamwise velocity (left) and u_{rms} (right) for the flow over the surface of the 35° slant using a wall model (WM) or zero-velocity Dirichlet boundary condition (NS).

Contrary to the better performance of the IDDES turbulence model for the 35° case compared to the CES, the IDDES can not reproduce the flow over the Ahmed body with the 25° slant angle according to the reference simulation and the experimental data. As it is seen in Fig. 22, the separation on the slant takes place with a delay and the detached boundary layer that extends into the wake. This behavior contradicts the discussed observations that the small separation bubble follows by a reattachment on the slant surface for the 25° case. The streamwise velocity and u_{rms} profiles around the body (Figs. 23 and 24) also confirm the presence of a fully detached boundary layer for the $\phi = 25°$, which leads to a wrong representation of the flow structures in the wake. As discussed before for the previous test case (see Section 3.2), this is probably related to the lack of sufficient local grid resolution to solve the boundary

flow components. The wall distance y^+ on the slant is around $100 - 150$. This value is large for resolving the small-scale eddies in the vicinity of the slant surface, though sufficiently small y^+ on the Cartesian grid leads to a significant increase in computational costs. However, in order to ensure the effects of this issue, it will be further considered and assessed in future research.

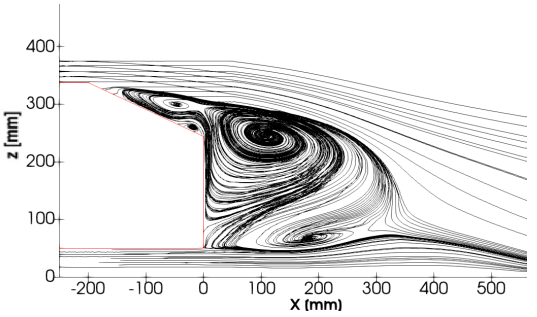

(a) IDDES (no-slip condition)

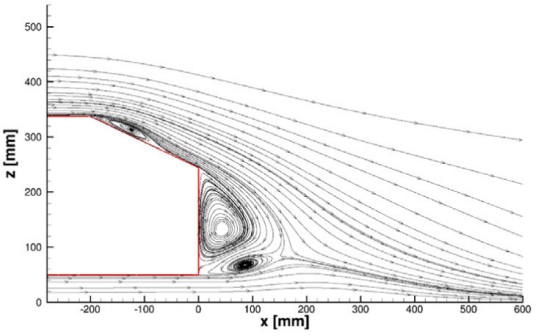

(b) reference IDDES [21]

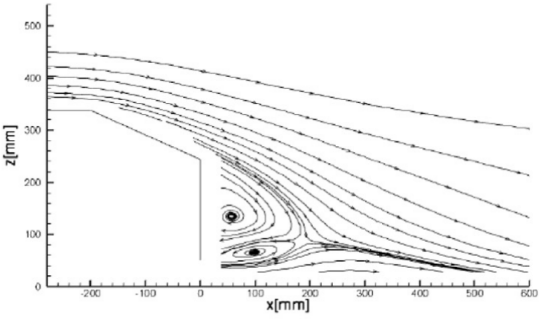

(c) Exp. [34]

Figure 22: Streamlines in the wake of the Ahmed body with 25° slant angle. The reference figures (b, c) were copied from [21] by permission.

Finally, the drag coefficients for all current simulations are summarized in Table 3 and compared to the experimental and numerical data. For this test case, the aerodynamic forces are strongly affected by the wake behind the body which is characterized by the separation region and counter-rotating vortices emitted from the slant side edges. For the IDDES simulation with the Dirichlet boundary condition, in which the wake is represented in a satisfactory way, the corresponding lift and drag coefficients are close to reference values. In other cases however, due to the inability of predicting local fluid dynamics (e.g. separation, reattachment), large discrepancies are observed between the predicted values and reference data.

4. Conclusion

The two-equation k-ω SST turbulence model and two hybrid RANS/LES models have been integrated in this study into the LBM framework. The performance of the k-ω SST RANS model has been compared with the widely used SA model for a two-dimensional flow over an airfoil. To further assess its accuracy and reliability, two k-ω SST based hybrid models IDDES and CES, have been investigated on an airfoil at different angles of attack from a fully attached condition to a highly unsteady forced stall. Although in all the simulations, an equilibrium wall model is applied as a near-wall treatment, the averaged solutions, including aerodynamic forces, are largely consistent with the reference data, even for states where the flow is not in equilibrium and under large adverse pressure gradients.

The simulation of flows around and in the wake of the Ahmed body, which is highly unsteady, three-dimensional, massively separated, and associated with complex turbulent coherent structures, well demonstrated the robustness of the hybrid turbulence models in conjunction with the LBM. For fully attached flow or massive separation triggered

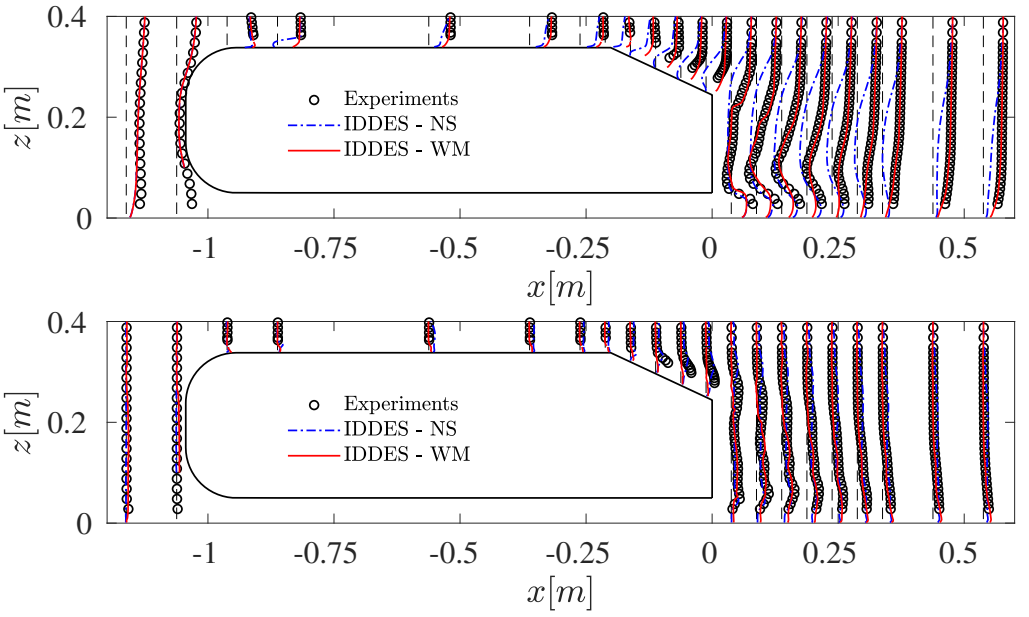

Figure 23: Comparison of the mean streamwise velocity (top) and u_{rms} (bottom) for the flow over the Ahmed body with 25° slant using a wall model (WM) or zero-velocity Dirichlet boundary condition (NS).

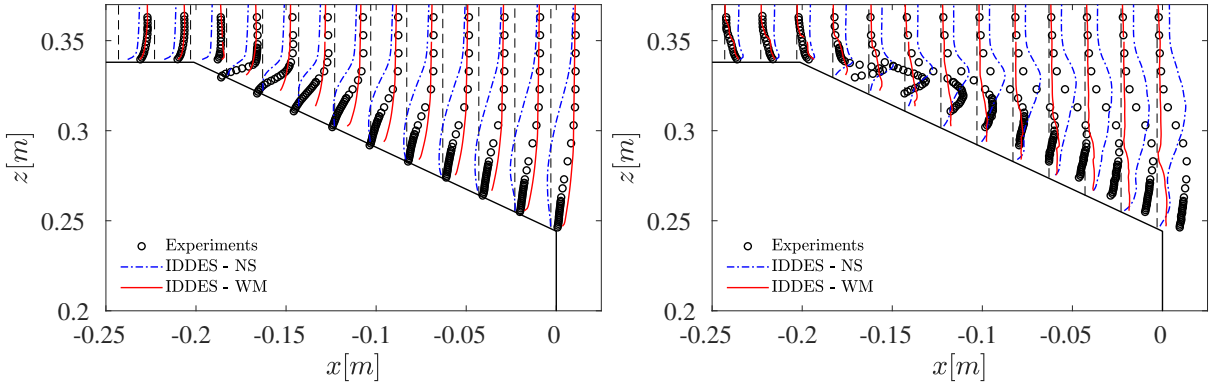

Figure 24: Comparison of the mean streamwise velocity (left) and u_{rms} (right) for the flow over the surface of the 25° slant using a wall model (WM) or zero-velocity Dirichlet boundary condition (NS).

by geometric singularities, the hybrid models can generally be used in combination with the equilibrium wall models with reliability. However, in the case of high adverse pressure gradient in the boundary layer and mild separation, these wall models may introduce some error in the prediction of flow features near the wall. One possible solution is to consider the effect of adverse pressure gradient inside the wall model formulation. As the next step of this work, the wall model proposed by Wilhelm et al. [63] will be applied in order to take into account the non-equilibrium effects in the near-wall treatment. Primary findings from the authors show that the adverse pressure gradients have substantial performance enhancements, notably for considerable boundary layer separation as exemplified by the Ahmed body case. To underscore the significant impact of wall modeling on the efficacy of these hybrid models in challenging and complex cases like the Ahmed body, the previous wall models were replaced by a non-zero Dirichlet velocity. This modification significantly altered the flow topology on the slanted surface, resulting in separated boundary layers along the slant as well as the top and sides of the body. For the CES, these separations in the beginning part of the body extended to the wake of the body and significantly affected the flow structures in the wake. In the IDDES simulation, as a result of the reattachment near the end of the slant, the local flow features and velocity profiles in the wake were in agreement with the references. For the case with 25° slant angle however, in addition to the delayed separation on

Table 3
Comparison of the drag coefficient for the Ahmed body at the slant angle of 25° and 35° with a wall model applied on the body surface (WM), or zero-Dirichlet boundary condition (NS).

	Method	Re_H	C_D 35°	C_D 25°
Ahmed et al. [1]	Experiment	1.2×10^6	0.2580	0.2850
Meile et al. [39]	Experiment	7.68×10^5	0.2790	0.2990
Liu et al. [35]	Experiment	1.4×10^5	0.32	n.a.
Thacker et al. [53]	Experiment	1.4×10^5	n.a.	0.3840
Guilmineau et al. [21]	$k-\omega$ SST- NS	7.68×10^5	0.2999	0.3218
	IDDES - NS	7.68×10^5	0.3452	0.3802
Present	IDDES - WM	7.68×10^5	0.2878	0.2510
	CES - WM	7.68×10^5	0.2738	-
	IDDES - NS	7.68×10^5	0.2819	0.2970
	CES - NS	7.68×10^5	0.3779	-

the slant, unlike the reference observation, no reattachment was captured. This can be due to the insufficient local grid resolution around the slant surface as the mesh was not originally designed to solve the flow parameters near the wall. This should also be considered in further studies of this work.

Acknowledgement

Centre de Calcul Intensif d'Aix-Marseille is acknowledged for granting access to its high-performance computing resources. This work was supported by ANR Industrial Chair ALBUMS (grant ANR-18-CHIN-0003-01) and by the French project BALBUZARD funded by DGAC and supported by Next generation EU in the frame of "Plan national de Relance et de Résilience français (PNRR)".

References

[1] Ahmed, S.R., Ramm, G., Faltin, G., 1984. Some salient features of the time-averaged ground vehicle wake. SAE Transactions 93, 473–503. doi:10.2307/44434262.

[2] Astoul, T., Wissocq, G., Boussuge, J.F., Sengissen, A., Sagaut, P., 2020. Analysis and reduction of spurious noise generated at grid refinement interfaces with the lattice Boltzmann method. Journal of Computational Physics 418, 109645. doi:10.1016/j.jcp.2020.109645.

[3] Boivin, P., Tayyab, M., Zhao, S., 2021. Benchmarking a lattice-Boltzmann solver for reactive flows: Is the method worth the effort for combustion? Physics of Fluids 33, 071703. doi:10.1063/5.0057352.

[4] Broeren, A.P., Addy, H.E., Lee, S., Monastero, M.C., 2014. Validation of 3-D ice accretion measurement methodology for experimental aerodynamic simulation, in: 6^{th} AIAA Atmospheric and Space Environments Conference, p. 2614. doi:10.2514/6.2014-2614.

[5] Buffa, E., Jacob, J., Sagaut, P., 2021. Lattice-Boltzmann-based large-eddy simulation of high-rise building aerodynamics with inlet turbulence reconstruction. Journal of Wind Engineering and Industrial Aerodynamics 212, 104560. doi:10.1016/j.jweia.2021.104560.

[6] Cai, S.G., Degrigny, J., Boussuge, J.F., Sagaut, P., 2021. Coupling of turbulence wall models and immersed boundaries on Cartesian grids. Journal of Computational Physics 429, 109995. doi:10.1016/j.jcp.2020.109995.

[7] Cai, S.G., Mozaffari, S., Jacob, J., Sagaut, P., 2022. Application of immersed boundary based turbulence wall modeling to the Ahmed body aerodynamics. Physics of Fluids 34, 095106. doi:10.1063/5.0098232.

[8] Cai, S.G., Sagaut, P., 2021. Explicit wall models for large eddy simulation. Physics of Fluids 33, 041703. doi:10.1007/s10494-020-00181-7.

[9] Cambier, L., Heib, S., Plot, S., 2013. The Onera elsA CFD software: input from research and feedback from industry. Mechanics & Industry 14, 159–174. doi:10.1051/meca/2013056.

[10] CS, 2017. ProLB website. http://www.prolb-cfd.com.

[11] Degrigny, J., Cai, S.G., Boussuge, J.F., Sagaut, P., 2021. Improved wall model treatment for aerodynamic flows in LBM. Computers & Fluids 227, 105041. doi:10.1016/j.compfluid.2021.105041.

[12] Degrigny, J., Pont, G., Boussuge, J.F., Sagaut, P., 2020. Simulation of high-lift flows through IDDES in LBM, in: 55^{th} 3AF International Conference on Applied Aerodynamics.

[13] Derksen, J., Van den Akker, H.E., 1999. Large eddy simulations on the flow driven by a Rushton turbine. AIChE Journal 45, 209–221. doi:10.1002/aic.690450202.

[14] Dong, Y.H., Sagaut, P., 2008. A study of time correlations in lattice Boltzmann-based large-eddy simulation of isotropic turbulence. Physics of Fluids 20, 035105. doi:10.1063/1.2842381.

[15] Dong, Z.Q., Wang, L.P., Peng, C., Chen, T., 2022. A systematic study of hidden errors in the bounce-back scheme and their various effects in the lattice Boltzmann simulation of viscous flows. Physics of Fluids 34, 093608. doi:10.1063/5.0106954.

[16] Drela, M., Youngren, H., 2001. Xfoil 6.94 user guide.

[17] Ducros, F., Nicoud, F., Poinsot, T., 1998. Wall-adapting local eddy-viscosity models for simulations in complex geometries. Numerical Methods for Fluid Dynamics VI , 293–299.

[18] ERCOFTAC, 2004. Ahmed body. URL: https://www.kbwiki.ercoftac.org/w/index.php/Description_AC1-05.

[19] Filippova, O., Succi, S., Mazzocco, F., Arrighetti, C., Bella, G., Hänel, D., 2001. Multiscale lattice Boltzmann schemes with turbulence modeling. Journal of Computational Physics 170, 812–829. doi:10.1006/jcph.2001.6764.

[20] Gritskevich, M.S., Garbaruk, A.V., Schütze, J., Menter, F.R., 2012. Development of DDES and IDDES formulations for the k-ω shear stress transport model. Flow, turbulence and combustion 88, 431–449. doi:10.1007/s10494-011-9378-4.

[21] Guilmineau, E., Deng, G., Leroyer, A., Queutey, P., Visonneau, M., Wackers, J., 2018. Assessment of hybrid RANS-LES formulations for flow simulation around the Ahmed body. Computers & Fluids 176, 302–319. doi:10.1016/j.compfluid.2017.01.005.

[22] Heinz, S., 2019. The large eddy simulation capability of Reynolds-averaged Navier-Stokes equations: Analytical results. Physics of Fluids 31, 021702. doi:10.1063/1.5085435.

[23] Heinz, S., 2020. A review of hybrid RANS-LES methods for turbulent flows: Concepts and applications. Progress in Aerospace Sciences 114, 100597. doi:10.1016/j.paerosci.2019.100597.

[24] Heinz, S., 2021. The continuous eddy simulation capability of velocity and scalar probability density function equations for turbulent flows. Physics of Fluids 33, 025107. doi:10.1063/5.0039163.

[25] Hou, S., Sterling, J., Chen, S., Doolen, G., 1994. A lattice Boltzmann subgrid model for high Reynolds number flows. arXiv preprint comp-gas/9401004 doi:10.48550/arXiv.comp-gas/9401004.

[26] Jacob, J., Malaspinas, O., Sagaut, P., 2018. A new hybrid recursive regularised Bhatnagar–Gross–Krook collision model for lattice Boltzmann method-based large eddy simulation. Journal of Turbulence 19, 1051–1076. doi:10.1080/14685248.2018.1540879.

[27] Kalitzin, G., Medic, G., Iaccarino, G., Durbin, P., 2005. Near-wall behavior of RANS turbulence models and implications for wall functions. Journal of Computational Physics 204, 265–291. doi:10.1016/j.jcp.2004.10.018.

[28] Knopp, T., Alrutz, T., Schwamborn, D., 2006. A grid and flow adaptive wall-function method for RANS turbulence modelling. Journal of Computational Physics 220, 19–40. doi:10.1016/j.jcp.2006.05.003.

[29] Krüger, T., Kusumaatmaja, H., Kuzmin, A., Shardt, O., Silva, G., Viggen, E.M., 2017. The lattice Boltzmann method. Springer International Publishing 10, 4–15. doi:10.1007/978-3-319-44649-3.

[30] Ladson, C.L., 1988. Effects of independent variation of Mach and Reynolds numbers on the low-speed aerodynamic characteristics of the NACA 0012 airfoil section. volume 4074.

[31] Ladson, C.L., Hill, A.S., Johnson Jr, W.G., 1987. Pressure distributions from high Reynolds number transonic tests of an NACA 0012 airfoil in the Langley 0.3-meter transonic cryogenic tunnel. Technical Report. NASA-TM-100526. langley Research Center, NASA.

[32] Lee, S., Bragg, M.B., 1999. Experimental investigation of simulated large-droplet ice shapes on airfoil aerodynamics. Journal of Aircraft 36, 844–850. doi:10.2514/2.2518.

[33] Li, K., Zhong, C., Zhuo, C., Cao, J., 2012. Non-body-fitted Cartesian-mesh simulation of highly turbulent flows using multi-relaxation-time lattice Boltzmann method. Computers & Mathematics with Applications 63, 1481–1496. doi:10.1016/j.camwa.2012.03.080.

[34] Lienhart, H., Becker, S., 2003. Flow and turbulence structure in the wake of a simplified car model. SAE transactions , 785–796URL: https://www.jstor.org/stable/44745451.

[35] Liu, K., Zhang, B., Zhang, Y., Zhou, Y., 2021. Flow structure around a low-drag Ahmed body. Journal of Fluid Mechanics 913. doi:10.1017/jfm.2020.1136.

[36] Liu, M., Chen, X.P., Premnath, K.N., 2012. Comparative study of the large eddy simulations with the lattice Boltzmann method using the wall-adapting local eddy-viscosity and Vreman subgrid scale models. Chinese Physics Letters 29, 104706. doi:10.1088/0256-307x/29/10/104706.

[37] Lu, Z., Liao, Y., Qian, D., McLaughlin, J., Derksen, J., Kontomaris, K., 2002. Large eddy simulations of a stirred tank using the lattice Boltzmann method on a nonuniform grid. Journal of Computational Physics 181, 675–704. doi:10.1006/jcph.2002.7151.

[38] Marié, S., Ricot, D., Sagaut, P., 2009. Comparison between lattice Boltzmann method and Navier–Stokes high order schemes for computational aeroacoustics. Journal of Computational Physics 228, 1056–1070. doi:10.1016/j.jcp.2008.10.021.

[39] Meile, W., Brenn, G., Reppenhagen, A., Lechner, B., Fuchs, A., 2011. Experiments and numerical simulations on the aerodynamics of the Ahmed body. CFD letters 3, 32–39.

[40] Menter, F.R., 1994. Two-equation eddy-viscosity turbulence models for engineering applications. AIAA journal 32, 1598–1605. doi:10.2514/3.12149.

[41] Menter, F.R., 2009. Review of the shear-stress transport turbulence model experience from an industrial perspective. International journal of computational fluid dynamics 23, 305–316. doi:10.1080/10618560902773387.

[42] Menter, F.R., Kuntz, M., 2004. Adaptation of eddy-viscosity turbulence models to unsteady separated flow behind vehicles, in: The aerodynamics of heavy vehicles: trucks, buses, and trains. Springer, pp. 339–352. doi:10.1007/978-3-540-44419-0_30.

[43] Pellerin, N., Leclaire, S., Reggio, M., 2015. An implementation of the Spalart–Allmaras turbulence model in a multi-domain lattice Boltzmann method for solving turbulent airfoil flows. Computers & Mathematics with Applications 70, 3001–3018. doi:10.1016/j.camwa.2015.10.006.

[44] Sajjadi, H., Salmanzadeh, M., Ahmadi, G., Jafari, S., 2017. Turbulent indoor airflow simulation using hybrid LES/RANS model utilizing

lattice Boltzmann method. Computers & Fluids 150, 66–73. doi:10.1016/j.compfluid.2017.03.028.
[45] Shur, M., Spalart, P., Strelets, M., Travin, A., 1999. Detached-eddy simulation of an airfoil at high angle of attack, in: Engineering turbulence modelling and experiments 4. Elsevier, pp. 669–678. doi:10.1016/B978-008043328-8/50064-3.
[46] Shur, M.L., Spalart, P.R., Strelets, M.K., Travin, A.K., 2008. A hybrid RANS-LES approach with delayed-DES and wall-modelled LES capabilities. International Journal of Heat and Fluid Flow 29, 1638–1649. doi:10.1016/j.ijheatfluidflow.2008.07.001.
[47] Spalart, P.R., 1997. Comments on the feasibility of LES for wings, and on a hybrid RANS/LES approach, in: Proceedings of first AFOSR international conference on DNS/LES, Greyden Press.
[48] Spalart, P.R., Allmaras, S., 1992. A one-equation turbulence model for aerodynamic flows, in: 30^{th} aerospace sciences meeting and exhibit, p. 439. doi:10.2514/6.1992-439.
[49] Spalart, P.R., Deck, S., Shur, M.L., Squires, K.D., Strelets, M.K., Travin, A.K., 2006. A new version of detached-eddy simulation, resistant to ambiguous grid densities. Theoretical and Computational Fluid Dynamics 20, 181–195. doi:10.1007/s00162-006-0015-0.
[50] Squires, K.D., Forsythe, J.R., Spalart, P.R., 2001. Detached-eddy simulation of the separated flow around a forebody cross-section, in: Direct and Large-Eddy Simulation IV. Springer, pp. 481–500. doi:10.1007/978-94-017-1263-7_57.
[51] Strelets, M.K., 2001. Detached eddy simulation of massively separated flows, in: 39^{th} Aerospace sciences meeting and exhibit, p. 879. doi:10.2514/6.2001-879.
[52] Suss, A., Mary, I., Le Garrec, T., Marié, S., 2023. Comprehensive comparison between the lattice Boltzmann and Navier–Stokes methods for aerodynamic and aeroacoustic applications. Computers & Fluids 257, 105881. doi:10.1016/j.compfluid.2023.105881.
[53] Thacker, A., Aubrun, S., Leroy, A., Devinant, P., 2012. Effects of suppressing the 3D separation on the rear slant on the flow structures around an Ahmed body. Journal of Wind Engineering and Industrial Aerodynamics 107, 237–243. doi:10.1016/j.jweia.2012.04.022.
[54] Travin, A.K., Shur, M.L., Strelets, M.K., Spalart, P.R., 2002. Physical and numerical upgrades in the detached-eddy simulation of complex turbulent flows, in: Advances in LES of complex flows. Springer, pp. 239–254. doi:10.1007/0-306-48383-1_16.
[55] Van Albada, G.D., Leer, B.v., Roberts, W., 1997. A comparative study of computational methods in cosmic gas dynamics, in: Upwind and high-resolution schemes. Springer, pp. 95–103. doi:10.1007/978-3-642-60543-7_6.
[56] Vreman, A., 2004. An eddy-viscosity subgrid-scale model for turbulent shear flow: Algebraic theory and applications. Physics of fluids 16, 3670–3681. doi:10.1063/1.1785131.
[57] Wang, Y., Zhong, C., Cao, J., Zhuo, C., Liu, S., 2020a. A simplified finite volume lattice Boltzmann method for simulations of fluid flows from laminar to turbulent regime, Part I: Numerical framework and its application to laminar flow simulation. Computers & Mathematics with Applications 79, 1590–1618. doi:10.1016/j.camwa.2019.09.017.
[58] Wang, Y., Zhong, C., Cao, J., Zhuo, C., Liu, S., 2020b. A simplified finite volume lattice Boltzmann method for simulations of fluid flows from laminar to turbulent regime, Part II: Extension towards turbulent flow simulation. Computers & Mathematics with Applications 79, 2133–2152. doi:10.1016/j.camwa.2019.10.014.
[59] Weickert, M., Teike, G., Schmidt, O., Sommerfeld, M., 2010. Investigation of the LES WALE turbulence model within the lattice Boltzmann framework. Computers & Mathematics with Applications 59, 2200–2214. doi:10.1016/j.camwa.2009.08.060.
[60] Wilcox, D.C., 2006. Turbulence modeling for CFD .
[61] Wilcox, D.C., 2008. Formulation of the k-ω turbulence model revisited. AIAA journal 46, 2823–2838. doi:10.2514/1.36541.
[62] Wilhelm, S., Jacob, J., Sagaut, P., 2018. An explicit power-law-based wall model for lattice Boltzmann method–Reynolds-averaged numerical simulations of the flow around airfoils. Physics of Fluids 30, 065111. doi:10.1063/1.5031764.
[63] Wilhelm, S., Jacob, J., Sagaut, P., 2021. A new explicit algebraic wall model for LES of turbulent flows under adverse pressure gradient. Flow, Turbulence and Combustion 106, 1–35. doi:10.1007/s10494-020-00181-7.
[64] Xu, H., Sagaut, P., 2013. Analysis of the absorbing layers for the weakly-compressible lattice Boltzmann methods. Journal of Computational Physics 245, 14–42. doi:10.1016/j.jcp.2013.02.051.
[65] Yu, H., Girimaji, S.S., Luo, L.S., 2005a. DNS and LES of decaying isotropic turbulence with and without frame rotation using lattice Boltzmann method. Journal of Computational Physics 209, 599–616. doi:10.1016/j.jcp.2005.03.022.
[66] Yu, H., Girimaji, S.S., Luo, L.S., 2005b. Lattice Boltzmann simulations of decaying homogeneous isotropic turbulence. Physical Review E 71, 016708. doi:10.1103/PhysRevE.71.016708.
[67] Zhang, B., Zhou, Y., To, S., 2015. Unsteady flow structures around a high-drag Ahmed body. Journal of Fluid Mechanics 777, 291–326. doi:10.1017/jfm.2015.332.